1   **Behavioral-transcriptomic landscape of engineered T cells targeting human cancer**

2   **organoids**

3

4   **Authors:**

5   Johanna F. Dekkers[1,2,3#], Maria Alieva[2,3#], Astrid Cleven[4], Farid Keramati[2], Peter Brazda[2],

6   Heggert G. Rebel[2,3], Amber K.L. Wezenaar[2,3], Jens Puschhof[1,3], Maj-Britt Buchholz[2,3], Mario

7   Barrera Román[2,3], Inez Johanna[4], Angelo D. Meringa[4], Domenico Fasci[4], Maarten H. Geurts[1,3],

8   Hendrikus C.R. Ariese[2,3], Esmée J. van Vliet[2,3], Ravian L. van Ineveld[2,3], Effrosyni

9   Karaiskaki[4], Oded Kopper[1,3], Yotam E. Bar-Ephraim[1,3], Kai Kretzschmar[1,3], Alexander M.M.

10   Eggermont[2,5], Ellen J. Wehrens[2,3], Henk G. Stunnenberg[2], Hans Clevers[1,2,3±], Jürgen Kuball[4,6±],

11   Zsolt Sebestyen[4±] and Anne C. Rios[2,3±]

12

13   # These authors contributed equally to this work

14   ± These authors share senior authorship

15

16   **Affiliations:**

17   [1]Hubrecht Institute, Royal Netherlands Academy of Arts and Sciences (KNAW) and

18   University Medical Centre (UMC) Utrecht, Utrecht, The Netherlands.

19   [2]Princess Máxima Center for Pediatric Oncology, Utrecht, The Netherlands.

20   [3]Cancer Genomics Netherlands, Oncode Institute, Utrecht, the Netherlands.

21   [4]Center for Translational Immunology, UMC Utrecht, Utrecht University, Utrecht, The

22   Netherlands.

23   [5]UMC Utrecht, Utrecht, The Netherlands.

24   [6]Department of Hematology, UMC Utrecht, Utrecht University, Utrecht, The Netherlands

25   [*]Correspondence: a.c.rios@prinsesmaximacentrum.nl

Summary

Cellular immunotherapies are rapidly gaining clinical importance, yet predictive platforms for modeling their mode of action are lacking. Here, we developed a dynamic immuno-organoid 3D imaging-transcriptomics platform; BEHAV3D, to unravel the behavioral and underlying molecular mechanisms of solid tumor targeting. Applied to an emerging cancer metabolome-sensing immunotherapy: TEGs, we first demonstrate targeting of multiple breast cancer subtypes. Live-tracking of over 120,000 TEGs revealed a diverse behavioral landscape and identified a 'super engager' cluster with serial killing capability. Inference of single-cell behavior with transcriptomics identified the gene signature of 'super engager' killer TEGs, which contained 27 genes with no previously described T cell function. Furthermore, guided by a dynamic type 1 interferon (IFN-I) signaling module induced by high TEG-sensitive organoids, we show that IFN-I can prime resistant organoids for TEG-mediated killing. Thus, BEHAV3D characterizes behavioral-phenotypic heterogeneity of cellular immunotherapies and holds promise for improving solid tumor-targeting in a patient-specific manner.

Keywords:

BEHAV3D, multispectral time-lapse 3D imaging, behavioral classification, behavior-guided transcriptomics, patient-derived organoids (PDOs), breast cancer, T cell therapy, $\alpha\beta$ T cells engineered to express a Vγ9/Vδ2 T cell receptor (TEGs), breast cancer, serial killing

Introduction

Single-cell analyses are providing unprecedented opportunities to analyze the complexity of biological systems (van der Leun et al., 2020). However, they are restricted to providing a snapshot of cellular processes at a given timepoint. Yet living cells are highly dynamic, and their dynamic behavior shapes their function. Therefore, the development of technologies that address individual cell dynamics within a population is essential for understanding cellular behaviors and how these behaviors relate to function. Immune cells engineered to locate and kill tumor cells represent such dynamic cell populations with an increasing clinical importance (June and Sadelain, 2018). Successes of T cell therapies for hematological malignancies have sparked efforts to translate such approaches to solid tumors, including breast cancer (BC), but efficacy has so far been limited (Chen and Mellman, 2017). This poses a clear need for better understanding the mechanism of action of cellular therapies in order to optimize treatment design.

Because of challenges in identifying tumor-specific antigens for solid cancers (Schumacher et al., 2019), pan-tumor therapies that recognize metabolic alterations in cancer cells are being explored (Crowther et al., 2020). This includes an emerging therapy called TEGs, which are peripheral blood $\alpha\beta$ T cells engineered to express a Vγ9/Vδ2 T cell receptor (TCR), comprising both CD4$^+$ and CD8$^+$ subsets (Gründer et al., 2012; Johanna et al., 2019; Marcu-Malina et al., 2011; Sebestyen et al., 2019; Vyborova et al., 2020). These hybrid cells have the ability to recognize cancer cells via the Vγ9/Vδ2 TCR that senses metabolic changes through the recently identified ligand butyrophilin 2A1 (BTN2A1) bound to BTN3A1 (Rigau et al., 2020; Vyborova et al., 2020). Yet, they maintain the high proliferation and memory capacity of conventional $\alpha\beta$ T cells (Marcu-Malina et al., 2011). TEGs are currently in clinical trials for various

71   leukemia (Sebestyen et al., 2019), but their potential to target solid tumors remains unknown

72   and should be adressed in adequate preclinical models.

73

74   There is a growing interest to use organoid technology to model immunotherapy function (Bar-

75   Ephraim et al., 2019; Cattaneo et al., 2020; Neal et al., 2018; Schnalzger et al., 2019; Dijkstra

76   et al., 2018). Patient-derived organoids (PDOs) provide reliable *in vitro* human cancer models

77   that recapitulate important characteristics of the original tumor specimen (Tuveson et al.),

78   allowing for the study of patient-specifc therapy responses (Ganesh et al., 2019; Ooft et al.,

79   2019; Tiriac et al., 2018; Vlachogiannis et al., 2018; Yao et al., 2020). In addition, imaging has

80   proven to be a powerful approach to characterize the spatial cellular organization and tissue

81   dynamics in these 3D structures (Dekkers et al., 2019; van Ineveld et al., *in press*; Lukonin et

82   al., 2020; 2019; Serra et al., 2019). Here, we aim to combine organoid and 3D imaging

83   technology for the analysis of functional single cell behavior integrated with transcriptomic

84   profiling to decipher and manipulate the solid tumor-targeting strategy of engineered immune

85   cells (**Video S1**).

86

87   **Results**

88

89   **3D live-tracked TEG targeting efficacy**

90   We devised a multispectral 3D image-based platform; BEHAV3D, to live-track efficacy and

91   mode-of-action of cellular immunotherapy for ~60 human cancer organoid cultures

92   simultaneously (**Figures 1A-1C; Video S1**). Multiple real-time fluorescent dyes and nanobody

93   technology were implemented for single acquisition 4-fluorophore spectral 3D imaging of T

94   cell populations, organoids, and dead cells, allowing us to track single TEGs, individual

95   organoids and their death-dynamics over 24 h (**Figures 1B, 1C, and S1A-S1C**). We detected

96   a high variation of TEG-mediated killing efficacy in cultures derived from 14 BC patients

97   (**Figure 1D; Table S1**), and different targeting kinetics over time (**Figures 1E, 1F, and S1D-**

98   **S1F**), with percentages of dying PDOs ranging from near 0% (e.g. 34T) to 100% (e.g. 13T)

99   (**Figure 1F**). Pearson correlation analysis between imaging data and a commonly used cell

100   viability assay (**Figures S1G and S1H**), or interferon gamma (IFN-γ) secretion measured by

101   ELISA (**Figures S1I and S1J**), confirmed robustness of our imaging quantification method.

102   Among the 6 highest TEG-sensitive PDO cultures (above 50% dying organoids; **Figure 1F**),

103   we noted cultures derived from primary BC of distinct subtypes (triple negative breast cancer

104   (TNBC), human epidermal growth factor receptor 2 (HER2)$^+$, estrogen receptor (ER)$^+$, and

105   ER$^+$ progesterone receptor (PR)$^+$HER2$^+$) and from a metastasis derived from a HER2$^+$ primary

106   tumor (**Figures 1D and 1F**), supporting the potential of TEGs in targeting a broad spectrum of

107   BCs. Importantly, TEGs control the growth of PDO-derived breast tumors (TNBC primary

108   tumor and HER2$^+$ metastasis) in mouse xenograft models (**Figure 1G**), showing efficacy of

109   TEG for BC *in vivo*.

110

111   **PDO inflammatory features associate with TEG sensitivity**

112   Bulk RNA sequencing of PDOs revealed differentially expressed genes (DEGs) between the 6

113   lowest versus the 6 highest TEG-sensitive PDO cultures (**Table S2**), related to upregulated

114   cadherin signaling and steroid biosynthesis pathways in TEG-insensitive cultures, whereas

115   cytokine signaling, as well as extracellular matrix (ECM) organization, correlated with high

116   sensitivity to TEG therapy (**Figures 1H, and S1K-S1M**). The highest association was found

117   between TEG killing and type 1 interferon (IFN-I) signaling genes, including MX1, IFIT1,

118   OASL, and XAF1, which were highly expressed especially in the 2 highest TEG-sensitive PDO

119   cultures; 14T and 13T (**Figures 1H, and S1M**). Thus, PDOs maintain tumor-specific

120   inflammatory features in culture, highlighting their utility for modeling cellular

121   immunotherapy responses in a patient-specific manner.

122

123   **TEGs display a high diversity in behavior and killing potential**

124   BEHAV3D implements single immune cell tracking in a 3D space over time and behavioral

125   classification (**Figures 1B, and 2A; Video S1**), revealing that -when exposed to PDOs- TEGs

126   could be separated into nine subpopulations with unique behavioral patterns (**Figures 2B-2D,**

127   **and S2A, S2B**). Patterns varied from inactive behaviors (*dying*, *static* and *lazy*) to active

128   motility (*slow scanner*, *medium scanner* and *super scanner*) and organoid engagement (*tickler*,

129   *engager* and *super engager*), thus demonstrating a high level of behavioral heterogeneity.

130   Having captured their behavioral single-cell landscape in this classifier (**Figures S3C-S3E)**,

131   we next predicted TEG behavior when co-cultured with PDOs that showed varying TEG

132   sensitivity (34T, 100T, 27T, 10T or 13T; **Figure 1F**), as well as an organoid culture derived

133   from normal breast tissue, which only showed minimal death when cultured with TEGs

134   (**Figure 2E**). A total of 123,296 TEGs were live-tracked to investigate how the organoid

135   (inflammatory) profile shapes T cell behavior. For each PDO culture, TEGs displayed unique

136   distributions of behavioral signatures (**Figure 2E**) and higher organoid killing associated with

137   an increase in tumor engagement (*tickler*, *engager* and *super engager*), while *static, lazy* and

138   *medium scanner* behavior decreased (**Figure 2F**). Correlation between single organoid dying

139   dynamics and TEG engagement over time revealed that organoids contacted by *super*

140   *engagers*, as compared to other organoid-engaging clusters, had the highest chance of being

141   killed (**Figures 2G, and S2F).** This indicates that effective killing by TEGs relies on prolonged

142   organoid contact, a main feature of *super engagers* (48 ± 8 min / hr; mean $\pm$ s.d.).

143

144

Serial killing capability of *super engager* CD8$^+$ TEGs

We next linked behaviors to population phenotypes by first differentially labeling CD4$^+$ and and CD8$^+$ T cells **(Figures 3A, and S3A)**. This revealed that prolonged organoid contact and *super engager* behavior was a preferred feature of CD8$^+$ TEGs, whereas CD4$^+$ TEGs showed a higher proportion of *lazy* cells, *slow scanners*, *medium scanners*, *super scanners*, and *ticklers* **(Figures 3A-3C)** characteristic of high movement and short organoid contact **(Figure 2C)**. Furthermore, long-term behavior classification and back-projection of cells classified in the live-tracked imaging dataset **(Figures S3B and S3C)**, showed that single CD8$^+$ TEGs, once engaged with an organoid, most often killed multiple cells consecutively (serial killing) **(Figures 3D-3G)**, a preferred feature of engineered T cells(Cazaux et al., 2019; Halle et al., 2016; Weigelin et al.). In contrast, CD4$^+$ TEGs often moved away after organoid engagement without killing, but occasionally targeted individual cells in different organoids **(Figures 3D-3F, and S3D)** thereby displaying slower killing rates **(Figure 3H)**. Serial killing by *super engager* CD8$^+$ TEGs was characterized by attachment to PDOs using a defined anchor point from where surrounding cells were killed via long protrusions, intercalating between epithelial cells and extending their initial size up to 5 times **(Figures 3E, and S3E and S3F)**. Remarkably, single CD8$^+$ TEGs were able to kill entire organoids (up to 18 cells in 11 hrs; **Figures 3E and 3G; Video S1**). This extent of serial killing and morphological plasticity of *super engager* CD8$^+$ TEGs was uniquely revealed by the high spatiotemporal resolution character of BEHAV3D.

NCAM1 associates with *super engager* behavior

Through single cell RNA sequencing (scRNAseq), we observed differential expression of NCAM1 in CD8$^+$ TEGs **(Figures 3I, S3G and S3H; Table S3)**. Although linked to cytotoxicity in both αβ and γδ T cells(Van Acker et al., 2017), this surface marker has not been

170   examined in the context of cellular immunotherapy. We confirmed potent effector function

171   related to NCAM1 expression, by showing that NCAM1$^+$CD8$^+$ TEGs had a higher capacity to

172   kill 13T organoids compared to NCAM1$^-$CD8$^+$ TEGs (**Figure 3J**). To identify behavioral

173   mechanisms underlying this high killing potential, we pre-labeled CD8$^+$ TEGs with NCAM1

174   nanobodies (**Figure 3K)**, to directly compare NCAM1-positive and -negative populations

175   within the same environment. NCAM1$^+$CD8$^+$ TEGs showed reduced *dying* and *static* behavior

176   (**Figures 3L and 3M, and S3I**), supporting a higher *in vitro* persistence. Strikingly,

177   NCAM1$^+$CD8$^+$ TEGs additionally showed a significant increase in *super engager* behavior

178   compared to NCAM1$^-$CD8$^+$ TEGs (**Figure 3L and 3M**). Thus, surface marker expression can

179   be linked to engineered T cell behavior, offering the opportunity to enrich for potent effector

180   behaviors.

181

182   **Behavioral-transcriptomic profiling of TEGs**

183   To generate insight into the transcriptional programs that underlie tumor-targeting dynamics

184   revealed by BEHAV3D, we next performed single cell transcriptomic profiling of TEG

185   populations enriched for different behavioral signatures, including a TEG population

186   containing > 90% *super engagers* (**Figures 4A and 4B, and S4A; Video S1**). For each main

187   TEG subset, effector CD8$^+$ (CD8^{+eff}), effector CD4$^+$ (CD4^{+eff}) and memory CD4$^+$ (CD4^{+mem}),

188   profound transcriptional changes were observed upon 6 h co-culture with highly targeted 13T

189   organoids, as compared to baseline (*no target control*) (**Figures 4C-4E**), showing that dynamic

190   interplay with PDOs shapes the TEG transcriptomic profile. Behavioral probability mapping

191   inferred from pseudotemporal ordering (**Figure S4B**) of the sequenced TEG populations

192   (**Figure 4F**), revealed dynamic transcriptional programs that were highly conserved between

193   CD8^{+eff}, CD4^{+eff}, and CD4^{+mem} TEGs (**Figure 4G**; Gene cluster (CL)1-3; 85% of genes; **Table**

194   **S4**). These programs included genes to be down- (CL1) or up-regulated (CL3) by

195   environmental stimuli or engagement to PDOs, as well as genes transiently expressed (CL2)

196   along the pseudotime trajectory (**Figure 4G;** GO terms per CL in **Figure S4C**). This

197   differential dynamic expression matched with known gene function, confirming robust

198   ordering of TEGs, as shown by genes related to the CD3 signaling complex (LCK, SOS1,

199   CD3E, CD3G; CL1; GO term 'T cell activation'), known to be down-regulated upon T cell

200   activation(Liu et al., 2000) in CL1 (**Figure 4H**). NF-kB signaling, critical for tumor

201   control(Barnes et al., 2015), and effector molecules including FASLG, IFNG, GZMB, TNF

202   were found in CL3, with NF-kB signalling induced by environmental stimuli reaching

203   maximum expression upon prolonged PDO-engagement, while the effector molecules

204   appeared upon engagement (**Figure 4I**). In addition, CL3 contained genes related to rRNA

205   processing that only increased upon prolonged engagement with organoids (**Figure 4H**),

206   consistent with accelerated protein production in T cells following TCR engagement(Asmal et

207   al., 2003; Tan et al., 2017). Finally, CL2 contained early activation markers CD69 and EGR1

208   with peak expression upon short organoid engagement, in line with IL-2 (CL3), known to be

209   induced by EGR1(Collins et al., 2006), upregulated towards the end of the trajectory (**Figure**

210   **4I**). Thus, through our behavior-guided transcriptomics approach we robustly identified

211   dynamic gene orchestration of TEG during tumor targeting.

212

213   **Gene signature related to (serial) killing *super engager* TEGs**

214   Of gene sets regulated in a TEG subset-specific manner (CL4-8; 15% of genes), CL7 contained

215   genes mainly induced upon prolonged organoid engagement, including cytotoxic genes (e.g.

216   PRF1, CRTAM, XCL1) (**Figures 4H and 4I;** GO: 'Regulation of cell killing'). This cluster of

217   genes was specifically induced in *super engager* CD8^{+eff}, and to a lesser extent in CD4^{+eff}

218   TEGs, and almost absent in CD4^{+mem} TEGs (**Figure 4J**), associating this gene cluster with

219   potent (serial) killing T cells (**Figures 3D-3G**). Analysis of TEGs derived from a different

220 healthy donor and co-cultured with another PDO culture (10T), confirmed that 61 out of the

221 83 genes of CL7 represent a conserved 'killer' gene signature (**Table S5**). Of these, we

222 identified 20 genes related to T cell activation and cytotoxicity and 14 genes related to other T

223 cell functions (**Figures 4K, and S4D**). However, importantly, we found 27 genes with no

224 previously described T cell function (**Figures 4K, and S4D**). Overall, half of all conserved

225 signature genes (31/61) and 17 out of the 27 novel genes were related to morphological

226 plasticity processes, such as motility, cytoskeleton remodeling and adhesion (**Figure S4D**).

227 Given that morphological plasticity is a key determinant of cell migration, many of the novel

228 genes were found to have a role in promoting tumor cell migration and invasion, including

229 ECM production and mesenchymal state induction (HEG1, BZW2, DCAF13, SQLE, PKIA).

230 For some of these genes, such as CCT3 or AFAP1L2, the mechanism promoting migration is

231 yet undescribed. In line with the prolonged organoid engagement behavioral feature of *super*

232 *engager* TEGs (**Figure 2C**), we also found various genes related to cell adhesion, such as

233 NCEH1, BYSL or EMP1. Finally, some genes had an additional function related to neurite

234 outgrowth and dendritic pruning (SERPINE2, CHD4, NRTK1), potentially matching the long

235 protrusion that were observed to occur in these serial killing TEGs **(Figures 3E, and Figure**

236 **S3E and S3F; Video S1).** Thus, behavioral transcriptomics identified a specific gene signature

237 induced in (serial) killing *super engager* TEGs.

238

239 **PDOs shape the dynamic gene signature of TEG during tumor targeting**

240 To further explore our behavioral-guided transcriptomics approach, we next compared

241 behavior-enriched TEG populations co-cultured between either highly sensitive 13T or

242 intermediately targeted 10T PDOs. Distinct UMAP embedding of different TEG populations

243 (**Figure 5A**) indicated that the patient-specific organoid exposure influences the dynamic TEG

244 transcriptional profile. 41% or 61% of upregulated genes by environmental stimuli or upon

245 prolonged PDO engagement in *super engagers*, respectively, were common between 10T- and

246 13T-co-cultured TEGs (**Figures 5B**, **and S5A and S5B**; **Table S6**). Common *super engager-*

247 related gene signatures included rRNA processing, NF-kB signaling and cytokine signaling

248 (**Figure S5B**), and matched CL3 gene signatures (**Figure S4C**). However, 10T-co-cultured

249 TEGs were characterized by induction of high cytokine expression upon prolonged PDO

250 engagement, including TNF, IFNG and IL2, whereas IFN-I signaling genes were uniquely

251 induced in TEGs co-cultured with highly sensitive 13T (**Figures 5C, and S5C**).

252

253 **IFN-β primes PDOs for TEG mediated killing**

254 IFN-I signaling plays fundamental roles in anti-tumor immunity, yet with diverse and

255 sometimes opposing functions reported for both tumor and immune cells, thereby making it

256 difficult to fully comprehend and therapeutically exploit these effects(Boukhaled et al., 2021).

257 IFN-I signaling was detected in 13T organoids (**Figure S1M**), which most prominently

258 displayed increased RNA levels of the upstream mediator IFN-β, but not IFN-α, among our

259 collection of PDOs (**Figure 5D**). Secretion of IFN-β was confirmed by Luminex (**Figure S5D**),

260 implying that IFN-β was the main mediator of IFN-I signaling observed in 13T. Interestingly,

261 peak induction of IFN-I signaling in 13T-co-cultured TEGs was detected in non-organoid-

262 engaging TEGs (from *static* to *super scanner* behavior), in line with a secreted source of IFN-

263 β, while the pathway was shut down in *super engager* TEGs, suggesting a limited role of IFN-

264 I signaling in direct killing behavior (**Figures 4F-4H**). Adding recombinant IFN-β to co-

265 cultures of TEGs with various PDOs that showed low to medium sensitivity to TEG therapy

266 (100T, 34T, 27T and 10T) indeed did not affect TEG targeting efficacy (**Figure 5E**). However,

267 34T, 27T and 10T organoids pre-treated with IFN-β showed increased TEG-mediated killing,

268 while IFN-β treatment did not impact organoid viability by itself (**Figures 5F and 5G**). These

269 data support that IFN-β has limited impact on the killing capacity of *super engager* TEGs,

11

270   confirming that dynamic IFN-I signaling is mainly associating with *static* to *scanner* behavior.

271   Importantly however, IFN-I signaling increases the sensitivity of organoids to TEG therapy.

272   Thus, behavior-guided TEG transcriptomics in relation to the type of organoid exposure reveals

273   IFN-β to prime PDOs for targeting by TEGs. This illustrates the potential of the BEHAV3D to

274   better understand and guide combinatory treatment approaches in a patient-specific manner.

275

276

Discussion

Here, we provide an organoid-based 3D imaging-transcriptomic platform; BEHAV3D, for understanding the mode-of-action of cellular anti-cancer immunotherapies in a patient-specific manner. Using this pipeline, we report on the broad targeting potential of TEGs for breast cancer, poorly permissive to current immunotherapies (Esteva et al., 2019). In addition, by behavior-guided transcriptomics we have generated, to our knowledge, the first molecular map underlying the behavioral landscape of immune cells targeted to solid tumors. By exploiting these results, we were able to design an optimal sequence of IFN-I and TEG combination therapy to boost TEG organoid targeting.

Different from recent studies that have mapped the activation trajectories of murine immune cells during viral infection (Abbas et al., 2020), or human immune cells in normal physiology or cancer (Szabo et al., 2019), we here reconstructed activation trajectories for engineered T cells and uniquely exploited dynamic imaging data revealing their single-cell behavior. This allowed us to dissect gene programs induced by environmental stimuli, versus induction by short or prolonged tumor engagement, and thereby identify the gene signature of TEGs that (serially) killed tumor cells. This signature includes genes not previously linked to T cell function, thereby providing novel opportunities to potentially engineer next generation T cells with potent serial killing capability. Furthermore, multiple genes in this signature are associated with morphological plasticity. Such plasticity may underlie the remarkable cellular extensions of serial-killing TEGs, as observed in our 3D imaging data. Using these protrusions, TEGs intercalated between tumor cells while sequentially killing multiple tumor cells in the PDO, suggesting that morphological plasticity may be an important attribute in the targeting of solid tumors.

13

300   Type 1 IFNs have been described to be beneficial for the control of tumor growth,

301   including in breast cancer, either by exerting direct antitumor effects (Dunn et al., 2005), or by

302   improving the response to therapies, such as chemotherapy and checkpoint inhibition (Borden,

303   2019; Sistigu et al., 2014). Yet, opposite roles in inducing treatment resistance have been

304   described as well (Benci et al., 2016; Boukhaled et al., 2021; Jacquelot et al., 2019). By using

305   defined immune-organoid co-cultures, we have shown that an IFN-I signature intrinsic to

306   tumor cells associates with TEG sensitivity, and that IFN-β primes tumor cells for more

307   efficient targeting, rather than directly affecting TEG killing behavior. Thus, our data support

308   the clinical use of IFN-I in combination with TEGs and possibly other cellular

309   immunotherapies.

310   Adding to patient-specific drug responses observed in PDOs biobanks (Ganesh et al.,

311   2019; Jacob et al., 2020; Ooft et al., 2019; Tiriac et al., 2018; Vlachogiannis et al., 2018; Yao

312   et al., 2020), we show that not only killing efficacy, but also the underlying behavioral and

313   molecular mechanisms of cellular immunotherapy differ between different PDO cultures. We

314   even detected differences in killing dynamics between individual organoids belonging to the

315   same PDO culture. This demonstrates that our platform captures the inter- and intra-patient

316   heterogeneity, a major obstacle for treating solid tumors (Yamamoto et al., 2019). It is

317   intriguing that gene signatures induced in TEGs upon organoid engagement were partly

318   dictated by the type of PDO. In addition, the extent of IFN-β pre-treatment outcome on tumor

319   targeting differed between PDOs, with the highly resistant culture 100T remaining

320   unresponsive, whereas 34T displayed the highest (4-fold) increase in targeting. Together, these

321   findings warrant caution regarding generalizing the outcome of immuno-oncology studies that

322   use a single tumor model, and further supports the value of human organoid technology for

323   development of personalized therapies.

324   Altogether, BEHAV3D combines organoid, imaging and sequencing technologies to

325   offer a comprehensive platform that integrates multiple single-cell readouts, including tumor

326   death dynamics, single-cell behavior and underlying transcriptomic profiling (**Video S1**).

327   BEHAV3D may thus contribute to the efforts aimed at enhancing the efficacy of solid tumor-

328   targeting by cellular therapies.

329

330

331 **Methods**

332

333 **Human material**

334 All human PDO samples were retrieved from a biobank through the Hubrecht Organoid

335 Technology (HUB, www.hub4organoids.nl). Authorizations were obtained by the medical

336 ethical committee of UMC Utrecht (METC UMCU) at request of the HUB in order to ensure

337 compliance with the Dutch medical research involving human subjects' act. The normal

338 organoids were generated from milk obtained via the Moedermelkbank Amsterdam

339 (Amsterdam UMC). Informed consent was obtained from all donors.

340

341 **Animal material**

342 NOD.Cg-PrkdcscidIl2rgtm1Wjl/SzJ (NSG) mice purchased from Charles River Laboratories

343 (France). Experiments were conducted in accordance with Institutional Guidelines under

344 acquired permission from the local Ethical Committee and as per current Dutch laws on Animal

345 Experimentation. Mice were housed in sterile conditions using an individually ventilated cage

346 (IVC) system and fed with sterile food and water. Irradiated mice were given sterile water with

347 antibiotic ciproxin for the duration of the experiment. Mice were randomized with equal

348 distribution by age and initial weight measured on day 0 and divided into 10–15 mice per

349 group.

350

351 **Organoid culture**

352 Organoids were seeded in basement membrane extract (BME; Cultrex) in uncoated 12-well

353 plates (Greiner Bio-one) and cultured as described previously(Dekkers et al., 2021; Sachs et

354 al., 2017). Briefly, Advanced DMEM/F12 was supplemented with penicillin/streptomycin

355 (pen/strep), 10 mM HEPES, Glutamax (adDMEM/F12+++), 1 x B27 (all from Thermo Fisher),

356   1.25 mM N-acetyl-L-cysteine (Sigma-Aldrich), 10 mM Nicotinamide (Sigma-Aldrich), 5 μM

357   Y-27632 (Abmole), 5 nM Heregulin β-1 (Peprotech), 500 nM A83-01 (Tocris), 5 ng/ml EGF

358   (Peprotech), 20 ng/ml FGF-10 (Peprotech), 10% Noggin-conditioned medium (NCM)

359   (Cattaneo et al., 2020), 10% Rspo1-conditioned medium (RCM) (Broutier et al., 2016), and

360   0.1 mg/ml primocin (Thermo Fisher), and in addition with 1 μM SB202190 (Sigma-Aldrich)

361   and 5 ng/ml FGF-7 (Peprotech) for PDO propagation ('Type 1' culture medium(Dekkers et al.,

362   2021)), or with 20% Wnt3a-conditioned medium (WCM) (Broutier et al., 2016), 0.5 μg/ml

363   hydrocortisone (Sigma-Aldrich), 100 μM β-estradiol (Sigma-Aldrich) and 10 mM forskolin

364   (Sigma-Aldrich) for normal organoid propagation ('Type 2' culture medium (Dekkers et al.,

365   2021)). Culture medium was refreshed every 2–3 days and organoids were passaged 1:2–1:6

366   every 7–21 days using TrypLE Express (Thermo Fisher). For co-culturing, organoids of a 5–

367   12-day old culture (depending on PDO growth speed) were recovered from the BME by

368   resuspension in TrypLE Express and collected adDMEM/F12+++. The organoid suspension

369   was filtered through a 70 μm strainer (Greiner) to remove large organoids and pelleted before

370   co-culturing. Organoids of passage 5 to 30 after cell isolation were used.

371

372   **Cell lines**

373   Daudi (Gründer et al., 2012), HL60(Marcu-Malina et al., 2011) and Phoenix-Ampho cell lines

374   were obtained from ATCC (authenticated by short tandem repeat

375   profiling/karyotyping/isoenzyme analysis). Daudi and HL60 cells were cultured in RPMI

376   media supplemented with 10% fetal calf serum (FCS) and 1% pen/strep (all from Thermo

377   Fisher). Phoenix-Ampho cells were cultured in DMEM medium (Thermo Fisher)

378   supplemented with 10% FCS and 1% pen/strep. All cells were passaged for a maximum of 2

379   months, after which new seed stocks were thawed for experimental use. Furthermore, all cell

380   lines were routinely verified by growth rate, morphology, and/or flow cytometry and tested

381 negative for mycoplasma using MycoAlert Mycoplasma Kit. Peripheral blood mononuclear

382 cells (PBMCs) were obtained from Sanquin Blood bank (Amsterdam, The Netherlands) and

383 isolated using Ficoll gradient centrifugation methods from buffy coats.

384

Retroviral transduction of T cells

386 TEG001 (T cells engineered to express a highly tumor-reactive Vγ9Vδ2 TCR) (Gründer et al.,

387 2012; Straetemans et al., 2015; 2018), LM1s (mock T cells engineered to express a mutant

388 Vγ9/Vδ2 TCR with abrogated function) (Marcu-Malina et al., 2011), and TEG011 (mock T

389 cells engineered to express HLA-A*24:02-restricted Vγ5/Vδ1 TCR; used as control for *in vivo*

390 studies) (Kierkels et al., 2019; Scheper et al., 2013), were produced as previously described

391 (Marcu-Malina et al., 2011). Briefly, packaging cells (Phoenix-Ampho) were transfected with

392 helper constructs gag-pol (pHIT60), env (pCOLT-GALV) and pMP71 retroviral vectors

393 containing both Vγ9/Vδ2 TCR chains separated by a ribosomal skipping T2A sequence, using

394 FugeneHD reagent (Promega). Human PBMCs from healthy donors were pre-activated with

395 anti CD3 (30 ng/mL; Orthoclone OKT3; Janssen-Cilag) and IL-2 (50 IU/mL; Proleukin,

396 Novartis) and subsequently transduced twice with viral supernatant within 48 hrs in the

397 presence of 50 IU/mL IL-2 and 6 mg/mL polybrene (Sigma-Aldrich). TCR-transduced T cells

398 were expanded by stimulation with anti-CD3/CD28 Dynabeads (500,000 beads/10^6 cells; Life

399 Technologies) and IL-2 (50 IU/mL). Thereafter, TCR-transduced T cells were depleted of the

400 non-engineered T cells.

401

Depletion of non-engineered T cells

403 Depletion of non-engineered T cells was performed as previously described (Marcu-Malina et

404 al., 2011). In short, αβ T cells were transduced with pMP71: γ-T2A-δ and incubated with a

405 biotin-labelled anti-αβ TCR antibody (clone BW242/412; Miltenyi Biotec) followed by

406   incubation with an anti-biotin antibody coupled to magnetic beads (anti-biotin MicroBeads;

407   Miltenyi Biotec). Next, the cell suspension was applied onto an LD column and αβ TCR-

408   positive (αβ TCR$^+$) T cells were depleted by Magnetic-Activated Cell Sorting (MACS)

409   according to the manufacture's protocol (Miltenyi Biotec).

410

411   **Separation of CD4$^+$ and CD8$^+$ subsets of TEGs**

412   In order to separate CD4$^+$ and CD8$^+$ TEGs and LM1s, we performed positive selection using

413   either CD4 or CD8 Microbeads (Miltenyi Biotech) following manufacturer's instructions.

414   After incubation with magnetic microbeads cells were applied to LS columns and CD4$^+$ or

415   CD8$^+$ TEGs or LM1s were selected by MACS. After MACS selection procedure, both

416   Vγ9/Vδ2 TCR$^+$ CD4$^+$ or Vγ9/Vδ2 TCR$^+$ CD8$^+$ subsets of TEGs were separately expanded by

417   using a rapid expansion protocol (REP) (Marcu-Malina et al., 2011) where TEGs were cultured

418   in 'TEG culture medium' (RPMI-Glutamax supplemented with 2,5 – 10 % human serum

419   (Sanquin), 1% pen/strep and 0.5M beta-2- mercaptoethanol) on a feeder cell mixture

420   composing of irradiated allogenic PBMCs, Daudi and LCL-TM in the presence of IL2 (50

421   U/ml; Novartis Pharma), IL15 (5 ng/ml; R&D Systems) and PHA-L (1 μg/ml; Sigma-Aldrich).

422   TEGs were stimulated biweekly by using the REP protocol. In order to monitor the purity of

423   CD4$^+$ and CD8$^+$ TEGs, cells were analyzed by flow cytometry weekly prior to functional

424   assays by using anti-pan γδ TCR-PE (Beckman Coulter), anti- αβTCR-FITC (eBioscience),

425   anti-CD8-PerCP-Cy5.5 (Biolegend) and anti-CD4-APC (Biolegend) antibodies. TEGs with a

426   purity lower than 90% were re-selected as described above. TEGs were used for co-culture

427   assays 4 – 5 days after the last IL2/IL15/PHA-L stimulation.

428

429

430

Sorting of NCAM1$^{-/+}$ TEGs

CD8$^+$ TEGs were harvested at day 8-10 of their REP cycle, stained in flow cytometry (FC) buffer (2% fetal bovine serum, 1x PBS) with Hilyte-488-conjugated NCAM1 nanobodies (1:400; QVQ) and LIVE/DEAD Fixable Near-IR Dead Cell Stain (1:1000; ThermoFisher) for 30 minutes at 4°C and consecutively sorted using a SONY SH800S or a FACS Aria Cell Sorter (BD Biosciences) into NCAM1$^-$ and NCAM$^+$ populations. Cells were rested for 16 h in 'TEG culture medium' and then used for co-culture.

Live cell imaging of TEG and organoid co-cultures

LM1s or TEGs (20,000) were co-cultured with normal organoids, PDOs or control cell lines (Daudi or HL-60) in an effector to tumor cell (E:T) ratio of 1:3 or 1:25 (for **Figures 3D-3F**). CD4$^+$ and CD8$^+$ TEGs were mixed in a 1:1 ratio just before plating. Cells were incubated in 96-well glass-bottom SensoPlates (Greiner) in 200 µl 'co-culture medium': 50% 'Type 1' organoid culture medium, 50% 'TEG assay medium' (RPMI-Glutamax supplemented with 10% FCS and 1% pen/strep), 2.5% BME and pamidronate for the accumulation of the phosphoantigen IPP to stimulate tumor cell recognition(Marcu-Malina et al., 2011) (1:2000). 'Co-culture medium' was supplemented with both NucRed™ Dead 647 (2 drops per ml; Thermo Fisher) and TO-PRO-3 (1:3000; Thermo Fisher) for fluorescent labelling of living and dead cells ('Imaging medium'). Combination of NucRed™ Dead 647 and TO-PRO-3 light up dead cell when excited with the 633 nm laser, and living cells when excited with the 561 nm laser (**Figures S1A and S1B**). Both were combined to achieve the most optimal fluorescent intensity ratio between dead and living cells for live cell imaging. Prior to co-culturing, TEGs were incubated with eBioscience™ Cell Proliferation Dye eFluor™ 450 (referred to as eFluor-450; 1:4000; Thermo Fisher) in PBS for 10 min at 37 °C to fluorescently label all TEGs. When CD4$^+$ and CD8$^+$TEGs were simultaneously imaged, eFluor-450, as well as Calcein AM

456   (1:4000; Thermo Fisher) were used to label the different TEG subsets in PBS for 10 min at 37

457   °C. For NCAM1 pre-labeling experiments, a combination of eFluor-450 (1:4000; Thermo

458   Fisher) and Hilyte-488-conjugated NCAM1 nanobodies (1:400; QVQ) was used to label CD8$^+$

459   TEGs in PBS for 20 min at 37 °C prior to co-culturing. To prevent evaporation while imaging,

460   200 µl PBS was added to the wells surrounding the co-culture wells. The plate was placed in a

461   LSM880 (Zeiss) microscope containing an incubation chamber (37 °C; 5% CO_2) and incubated

462   for 30 min to ensure settling of TEGs and organoids at the bottom of the well. The plate was

463   imaged for up to 24 hrs with a Plan-Apochromat 20 x/0.8 NA dry objective with the following

464   settings: online fingerprinting mode, bidirectional scanning, optimal Z-stack step size, Z-stack

465   of 60 µm in total and time series with a 30 min (up to 60 conditions simultaneously; resolution

466   512 x 512) or 2 min interval (up to 4 or 10 conditions simultaneously; resolution 512 x 512 and

467   200 x 200 respectively). To minimize photobleaching of NCAM1-pre-labeled TEGs, the 488

468   nm laser was only activated 1 Z-stack each hr within the first hrs of imaging. Directly after

469   imaging, the production of IFN-γ in the supernatant was quantitated using an ELISA-ready-

470   go! Kit (eBioscience) and cell pellets were used to measure organoid viability using a CellTiter-

471   Glo® Luminescent Cell Viability Assay (Promega).

472

473   **IFN-β stimulations**

474   PDOs were harvested as described above and incubated in 96-well round bottom culture plates

475   (Thermo Fisher) in 100 µl 'Type 1' organoid culture medium, supplemented with 2.5% BME,

476   with or without the presence of 100 pg/ml recombinant human IFN-β (Peprotech). After 24 h

477   incubation (37 °C; 5% CO_2), TEGs or LM1s were added to either IFN-β-preincubated or

478   unstimulated organoids (E:T ratio of 1:3) in 100 µl 'TEG assay medium', supplemented with

479   2.5% BME and pamidronate (1:1000), with or without the presence of 100 pg/ml recombinant

480   human IFN-β (Peprotech). Medium without T cells was added for 'organoid only' controls.

481   After 16 h incubation (37 °C; 5% CO_2), plates were used to measure organoid viability using

482   a CellTiter-Glo® Luminescent Cell Viability Assay (Promega).

483

484   *In vivo* **targeting by TEGs**

485   Adult female NSG mice (15-16 weeks old) received sub-lethal total body irradiation (1,75 Gy)

486   and subcutaneous implantation of an β-estradiol pellet (Innovative Research of America) on

487   Day -1. On day 0, PDOs ($1x10^6$ 13T organoid cells in 100 μl BME per mouse) were prepared

488   as described previously (Dekkers et al., 2021) for subcutaneous injection on the right flank on

489   Day 0, and received 2 injections of 10^7 TEGs or TEG011 mock cells on day 1 and 6 in

490   pamidronate (10 mg/kg body weight) as previously reported(Johanna et al., 2019). On day 1,

491   together with the first T cell injection, all mice also received $0.6x10^6$ IU of IL-2 (Proleukin;

492   Novartis) in IFA subcutaneously. Tumor volume was measured once a week using digital

493   caliper and was calculated by the following formula: 0.4 x (length x width x width). Mice were

494   monitored at least twice a week for weight loss and clinical appearance scoring (scoring

495   parameter   included   hunched   appearance,   activity,   fur   texture,   piloerection,

496   respiratory/breathing problem). Humane endpoint (HEP) was reached when mice experienced

497   a 20% weight loss from the initial weight, tumor volume reached 2 cm^3, or when clinical

498   appearance score of 2 was reached for individual parameter or an overall score of 4.

499

500   **Image processing**

501   For 3D visualization, cell segmentation and extraction of statistics, time-lapse movies were

502   processed with Imaris (Oxford Instruments), versions 9.2 to 9.5. The *Channel Arithmetics*

503   Xtension was used for creating new channels to specifically identify organoids (live and dead)

504   and eFluor-450-labeled or calcein AM-labeled TEGs (live and dead) and exclude cell debris.

505   The Surface and ImarisTrack modules were used for object detection and automated tracking

506   of both TEGs (autoregressive motion) and organoids ('connected components' or no tracking).

507   The *Distance Transformation* Xtension was used to measure the distance between TEGs and

508   organoids and thresholds for defining organoid–T cell interactions were visually determined.

509   For tracked TEGs, time-lapse data containing the coordinates of each cell, the values of cell

510   speed, mean square displacement, distance to organoids and dead cell dye channel intensity

511   were exported. For experiments with NCAM1 pre-labelling, the mean intensities of the

512   NCAM1 channel per T cell were exported. For tracked organoids, time-lapse data containing

513   the coordinates of each organoid, the surface area, volume and mean dead cell dye channel

514   intensity were exported.

515

516   **Imaging and sequencing data processing**

517   Analysis of imaging and sequencing data was performed using R Studio version 4.0.2, as well

518   as the following R packages: DESeq2, devtools, dplyr, dtwclust, eulerr, gganimate, ggplot2,

519   ggpubr, ggrepel, gridExtra, hypergeo, kmodR, lme4, lmerTest, MESS, nlme, openxlsx,

520   parallel, patternplot, pheatmap, plotly, plyr, png, purr, RColorBrewer, readxl, reshape2, rgeos,

521   scales, Seurat, sp, spatstat, stats, tidyr, tidyverse, umap, VennDiagram, viridis, xlsx, zoo.

522

523   **PDOs killing dynamics**

524   To quantify cell death dynamics of PDO cultures, > 5000 single organoids were analyzed at

525   each time-point (48 time-points total). The mean dead cell dye intensity within single organoid

526   surfaces, and values were rescaled to a range between 0 and 100 per experiment to normalize

527   for variation in the absolute dead cell dye intensity. Per time point, organoids were classified

528   as 'dying' when the mean dead cell dye intensity was above 7.

529

530

T cell dynamics analysis and multivariate time series clustering

For the analysis of TEG behavior overtime, the following parameters were used: T cell death, contact with organoids, speed, square displacement and interaction with other T cells. Interactions between TEGs were measured by computing the distance to the nearest neighbor for each cell. To only include active interactions between TEGs that were not engaged to organoids, we considered cells whose mean speed for the last 20 minutes fell within the 3rd quartile. A threshold for interacting T cells was defined as 10 μm between cell centroids and confirmed by visual inspection of imaging data. For each TEG time series, linear interpolation was used to estimate the values in few cases of missing time points. To compare time series independently of their length, cell tracks were cut to a length of 3.3 hrs. For each experimental replicate, the values of each of the numeric variables were converted to z-scores. To enhance the most discrepant values, only the 3rd quartile range values were kept, while the rest was converted to the minimum values. Finally, each numeric variable was scaled to a range between 0 and 1 and normalized to the mean of the 0.99 quantile (per experimental replicate). For binary variables (TEG-TEG or TEG-organoid interactions), the values were labelled as 1 or 0 for interaction or no-interaction terms. Similarity between distinct cell tracks was measured using a strategy that allows for best alignment between time-series, previously applied for mitotic kinetics (Cai et al., 2018) or temporal module dynamics comparisons (Schafer et al., 2019). A cross-distance matrix based on the multivariate time-series data was computed using the dynamic time warping algorithm from the package "dtwclust". To visualize distinct cell behaviors in 2 dimensions, dimensionality reduction on the multidimensional feature count table was performed by Uniform Manifold Approximation and Projection method ("umap" package) (Ali et al.; Becht et al., 2018). Clustering was performed using the k-means clustering algorithm with outlier detection. The identity of each cluster was defined by the mean time-series values of the different parameters (speed, square displacement, organoid contact, T cell

556   interactions, cell death) within each cluster (**Figure 2C**). To confirm the identity of each

557   cluster, T cell cluster assignments were back-projected to visualize the surfaces and tracks of

558   particular T cell populations in the imaging dataset (**Figures 2A, S2A and S2B, and S3B**). A

559   combination of datasets with distinct behavioral characteristics was used to construct a global

560   TEG behavior atlas using the described methodology (**Figure 2B**).

561

562   **Cell behavior classification using a Random Forest classifier**

563   For standardized integration of new experiments, we used a random forest classification

564   approach (Breiman, L., 2001) in order to relate cell behavior to the nine behavioral signatures

565   that we found in our global TEG behavior atlas (**Figure 2B**). To allow for inclusion of

566   experiments with a low E:T ratio of 1:25, where the parameter of T cell interaction would be

567   influenced as compared to the standard E:T ratio of 1:3, the following parameters were used:

568   T cell death, organoid contact, speed, square displacement. The reference dataset used to build

569   the global TEG behavior atlas was split into cell tracks to be used as a training dataset (95%)

570   and a test dataset (5%). To reduce dimensionality, for each cell track, four time-series

571   descriptive statistics were quantified and used to train the classifier. For numeric variables, the

572   following measures were computed for each cell track: mean, median, the top 90% of the

573   distribution, and the standard deviation. For binary values, such as the contact with organoids,

574   the mean was calculated, as well as the mean and maximum of cumulative interaction. The

575   random forest classifier was trained using 100 trees on the above-mentioned variables using

576   the nine behavioral signatures as labels (**Figures S2C and S2D**). The test dataset was used to

577   assess for accuracy of the classifier and to determine in which behavioral signatures the errors

578   occurred (**Figure S2E**).

579

580

Correlation between TEG behavior and organoid killing dynamics

581 To estimate the correlation between the onset of death in individual organoids and the

583 engagement with T cells belonging to the engaging clusters (C7-9), we implemented a

584 technique of sliding window correlation analysis, previously used for functional brain

585 connectivity (Preti et al., 2017) and genome analysis (Burke et al., 2010). We calculated the

586 Pearson correlation coefficient between the cumulative number of organoid contacts with

587 TEGs from each cluster and the increase in dead cell dye intensity in each over a sliding

588 window of 3 hrs (**Figures 2F and S2F**).

589

590 **T cell serial killing capacity analysis**

591 For accurate long-term (up to 24 h) T cell tracking, TEGs were plated at a E:T ratio of 1:25.

592 Tracks were manually corrected where required. Tracks were divided into shorter subtracks of

593 160 minutes. Using the random forest classifier described above, each subtrack was assigned

594 to a behavioral signature (**Figures S2D and S2E**). The following statistics were calculated for

595 each type of behavioral signature (9 clusters): for continuous variables (square displacement;

596 speed, T cell death) the mean, median and standard deviation of the upper quantile were

597 calculated, and for discrete variables (organoid contact and interaction with T cells) the mean,

598 cumulative mean, maximum and cumulative maximum were calculated. Principal component

599 (PC) analysis was used to reduce the dimensionality. The top 5 PCs were used to classify the

600 change in behavioral signature over time (**Figures S3B and S3C**). Equivalent to the approach

601 that was used for the full tracks in **Figure 2B**, we computed a cross-distance matrix based on

602 the multivariate time-series data using the dynamic time warping algorithm and performed k-

603 means clustering in UMAP space. The change in behavioral signatures was represented in a

604 time-series color plot where each row represents one cell track and the color codes for

605 behavioral signature (**Figure S3C**). The relative proportion of CD4$^+$ and CD8$^+$ TEGs in each

606 cluster was calculated and plotted next to each long-term classification (**Figure S3C**).

607 TEGs that engaged to organoids were back-projected to the imaging dataset and their

608 first and second actions upon organoid engagement were visually analyzed (**Figure 3D**). TEG

609 morphological plasticity was calculated by measuring the cell elongation (ratio between the

610 longest and shortest axes) per cell and per individual timepoint. For each cell track, the

611 plasticity was then computed as the ratio between the maximal and the minimal cell elongation

612 (**Figure S3F**). The actions of CD4$^+$ and CD8$^+$ TEGs upon organoid engagement (**Figure 3D**)

613 as well as the speed of killing and serial killing potential (**Figures 3G and 3H**) were quantified

614 using Imaris software. Only TEGs were included for which tumor cell killing was clearly

615 observed (usually visible as a decrease in living cell dye and an increase in dead cell dye, which

616 co-occurred in many cases with target cell detachment from the organoid). For cases where a

617 single organoid was fully killed by a single TEG, the number of cells killed by the TEG was

618 calculated by dividing the killed volume by the average volume of a single 13T cell (2182

619 μm^3). The killing rate of TEGs was measured as the time period from target cell engagement

620 until tumor cell death (**Figure 3H**).

621

622 **NCAM1 pre-labelling quantification using 3D imaging data**

623 Behavioral classification of NCAM1 pre-labelled TEGs was performed as described above, by

624 predicting behavioral signatures with the Random Forest classifier. NCAM1$^{+/-}$ TEGs were

625 identified based on an NCAM1 intensity threshold in individual TEGs, visually defined at the

626 timepoints where the 488 nm laser was turned on. To ensure inclusion of true NCAM1$^-$ or

627 NCAM1$^+$ TEGs, two intensity thresholds were defined. Only tracks with a defined NCAM1$^+$

628 or NCAM1$^-$ identity were used for subsequent analysis. For each individual well, a difference

629 in percentage of NCAM1$^+$ and NCAM1$^-$ TEGs was calculated per behavioral signature

630 (**Figures 3L and S3I**).

631

632 **PDO bulk RNA sequencing**

633 For bulk RNA sequencing characterization, RNA of PDOs grown in 'Type 1' culture medium

634 was isolated according to the manufacturer's protocol using the RNeasy Mini Kit (QIAGEN).

635 Quality and quantity of the RNA samples and the libraries were measured with Agilent's

636 Bioanalyzer2100 and Invitrogen™ Qubit™ 3.0 Fluorometer. Quality control was done using

637 FastQC, alignment has been done using STAR

638 (https://github.com/alexdobin/STAR/releases/tag/STAR_2.4.2a) and reads have been mapped

639 to the GRCh37 version of the human reference genome. Quality control on the bams was done

640 using Picard. Read counts were generated with Htseq-count after which normalization is done

641 using DESeq. RPKMs have been calculated with edgeR. For the library preparation the TruSeq

642 Stranded mRNA Library Prep kit from Illumina was used. Sequencing was performed on the

643 nextseq500 sequencer (also Illumina) with single-end 75bp reads. PDO cultures were ranked

644 by responsiveness to TEGs (**Figure 1D**) and differentially expressed genes between the 6 most

645 TEG-sensitive and 6 least TEG-sensitive cultures were analyzed. Genes exhibiting a more than

646 4-fold expression change with an adjusted p-value <0.05 after multiple hypothesis testing

647 correction were used as input gene set enrichment analysis.

648

649 **SORTseq sample preparation**

650 For sequencing of different behavior-enriched TEG populations (**Figure 4A**), TEGs

651 (>0,8x10^6 per condition) were either (1) co-cultured with 13T PDOs (E:T of 1:3) and separated

652 into organoid-engaged (*engaged*) and organoid non-engaged (*non-engaged*) populations by 2

653 slow-spin (30 rcf) centrifugation steps at 6 h co-culture, (2) co-cultured with 10T or 13T PDOs

654 (E:T of 1: 3) and separated at 4 hrs into organoid-engaged and organoid non-engaged

655 populations by a slow-spin (30 rcf) centrifugation step, co-cultured for another 2h with or

656 without addition of fresh PDOs, again followed 2 slow-spin (30 rcf) centrifugation steps to

657 obtain *non-engaged*^{Enriched} and *super-engaged* TEG populations, or (3) cultured for six hrs

658 without addition of PDOs (*no target control*), using 12-wells culture plates (Thermo Fischer)

659 and 'co-culture medium'. To create single-cell suspensions, conditions containing organoids

660 (all '*engaged'* TEG conditions) were treated with TrypLE for seven minutes at 37°C and

661 washed with adDMEM/F12+++. Cells were then stained in FC buffer (2% FCS in

662 PBS) with anti-CD3-APC conjugated antibodies (1:80; BioLegend) and LIVE/DEAD Fixable

663 Near-IR Dead Cell Stain (1:1000; ThermoFisher) for 30 minutes at 4°C and sorted into 384-

664 wells SORTseq plates using a FACS Aria Cell Sorter (BD Biosciences) and directly stored at

665 -80°C until further processing.

666

667 **SORTseq library preparation and sequencing**

668 All sorted plates were processed according to the CEL-Seq2 protocol with the total

669 transcriptome amplification via poly-A RNA-capture, library preparation, and sequencing into

670 Illumina sequencing libraries as previously described(Muraro et al., 2016). Paired-end

671 sequencing (read1: 30 bp; read2: 120 bp) was used to sequence the prepared libraries using an

672 Illumina NextSeq sequencer.

673

674 **Mapping and quantification of SORTseq data**

675 SORTseq data were mapped and reads were counted, using STAR version 2.6.1a on the

676 Hg38p10 human genome (annotated with GenCode v26). Plate-QC was performed using the

677 Sharq pipeline (Candelli et al., 2018). Percentage of ERCC spike-in reads and mitochondrial

678 mRNA reads versus total read count per cell were applied as QC parameters to identify

679   systemic processing or pipetting errors over the plates. Cells with mitochondrial mRNA reads

680   higher than 15%, ribosomal RNA content higher than 30%, or ERCC reads higher than 25%

681   were excluded from the downstream analysis. Cells with fewer than 650 and higher than 4500

682   genes captured, and genes captured in fewer than 2 cells per plate were also excluded. After

683   the initial QC steps, the ERCC spike-in reads were removed from the final count tables.

684

685   **SORTseq and 10x genomics data integration and TEG subpopulation analysis**

686   For analysis of TEGs not exposed to organoids (**Figures 3I, and S3G and S3H**), 3

687   experimental replicates were used consisting of two datasets processed using SORT-seq and

688   one dataset processed using 10x Genomics Chromium Single Cell 3′ gene-expression kit.

689   SORTseq data was processed as described above. For the 10x dataset, (fresh, not co-cultured)

690   TEGs were viability-enriched via FACS by DAPI staining (1:1000; Thermo Fischer) and

691   loaded according to the standard protocol of the Chromium Single Cell 3′ Kit (v3). All the

692   following steps were performed according to the standard manufacturer's protocol. The library

693   was sequenced on an Illumina Novaseq S1-flowcell and 19,000 reads/cell were collected.

694   Single-cell RNAseq data were mapped, and counts of molecules per barcode were quantified

695   using the cellranger(3.1.0) 10x software package to map sequencing data to the GRCh38(3.0.0)

696   reference transcriptome supplied by 10x. Cells with mitochondrial mRNA reads higher than

697   15% and with fewer than 200 or more than 5000 distinct genes were excluded from the

698   downstream analysis. Data were normalized by sequencing depth, scaled to 10,000 counts, log-

699   transformed, and regressed against the UMI-counts and percentage of mitochondrial mRNA

700   using the ScaleData function of the Seurat package. For integration of the 10x genomics (n =

701   1) and SORTseq (n = 2) datasets, we used previously published Seurat v3 data anchor-based

702   integration(Stuart et al., 2019). Briefly, all three datasets were normalized using SCTtransform

703   (Hafemeister and Satija, 2019) followed by selection of 5000 features for downstream

704 integration. Transfer anchors were then learned and applied for integration of all datasets into

705 a combined dataset. Cell visualization and placement in 2D view was achieved using principal

706 component analysis (PCA) followed by Uniform Manifold Approximation and Projection

707 (UMAP)(McInnes et al.). Shared nearest neighbor graph-based clustering was done using

708 Seurat package's FindNeighbors and FindClusters functions with a resolution of 0.8. For cell

709 type identification marker genes for each cluster were calculated using the FindAllMarkers

710 function and examined to profile marker genes that correspond to known cell types. Additional

711 support for identifying cell subpopulations similitudes was achieved by analyzing the

712 differentially expressed genes with a cell-type annotation tool(Cao et al.). Main marker genes

713 used for TEG subpopulations identification are plotted in **Figure S3H.**

714

715 **Pseudotime Trajectory Inference**

716 Two experimental SORTseq replicates of TEGs co-cultured with 13T PDOs, generated as

717 described above, were used for trajectory interference (**Figure S4B)**. Proliferating T cells were

718 excluded from the analysis since they did not show any dynamic inflammatory genes during

719 the analysis. Afterwards, the gene expression table was log normalized with 10,000 scaling

720 factor. Cell visualization and placement in 2D view was achieved using principal component

721 analysis (PCA) followed by Uniform Manifold Approximation and Projection (UMAP)

722 (McInnes et al., 2020). Shared nearest neighbor graph-based clustering was done using Seurat

723 package's FindNeighbors and FindClusters functions with the resolution of 2. Based on marker

724 gene expression of CD8, CD4 and IL17RB (Terrier et al., 2010), TEGs were sub-clustered into

725 3 subtypes; IL17RB$^-$CD8^{+eff}, IL17RB$^-$CD4^{+eff} and IL17RB$^+$CD4^{+mem}. Downstream analyses

726 were done on each subset separately and compared with each other where mentioned.

727 RunFastMNN function from SeuratWrappers package was utilized to correct for batch effects

728 between the two SORTseq replicates. Unless specified, batch corrected UMAP values were

729   used for visualization of single cells. We used Monocle3 (Cao et al., 2020) package to infer the

730   pseudotime trajectory and significantly dynamic genes for each T cell subtype. For each cell

731   subtype either *no target control* or *non-engaged*^{Enriched} TEGs were designated as the root of the

732   trajectory. In order to have comparable results from both Seurat and Monocle3 packages, the

733   FastMNN batch corrected UMAP coordinates were imported and used throughout the

734   trajectory analysis in Monocle3. In IL17RB^{-}CD4^{+eff} and IL17RB^{+}CD4^{+mem} subtypes, Monocle

735   identified *no target control* cells as a separate partition. In order to have all cells along with a

736   single pseudotime spectrum (e.g., not having several cells with a same pseudotime value), we

737   added maximum pseudotime values of *no target control* T cells to pseudotime values of

738   remaining cells in that subtype. For all TEG subtypes, significant dynamic genes along with

739   the pseudotime trajectory were calculated and identified using Monocle3's graph_test function

740   using 1e-20 *q* value as the significance cutoff. Afterwards, using k-means clustering and also

741   visual inspection of the genes' behavior over the pseudotime, TEGs were clustered into sub-

742   clusters with similar pattern (CL1-8; **Figure 4G**). The expression profile of the genes along

743   with the pseudotime trajectory was plotted using pheatmap package(Kolde et al.) using row

744   scaled (z-score) expression values. Smoothed gene(s) behavior was calculated and visualized

745   recruiting gam smoothing function in ggplot2 package (Wilkinson, 2011).

746

747   **Behavior signature inference over the pseudotime.**

748   To align the pseudotime inference with the different behavioral signatures that we identified

749   with BEHAV3D, we build a probability map distribution for different behavioral signatures

750   over the pseudotime, based on the fundamental principle of transitivity of probabilistic

751   distribution (**Figure 4F**). We defined three states of cells quantified by different methods:

752   • Behavioral_signatures (B_{sig}): {*Static, Lazy, Medium-scanner, Scanner, Super scanner,*

753   *Tickler, Engager, Super engager*}. Behavioral signatures of cells identified by imaging

754   (**Figure 4B**).

755   • Experimental_engagement_state (Exp_{eng}): {*No target control, Non-engaged, Non-*

756   *engaged^{enriched}, Engaged, Super-engaged*}. Cell distribution among different

757   experimental conditions (**Figure 4A**)

758   • UMAP_cluster (U_{cl}): {1…X}. Cell assignment to distinct clusters grouping cells with

759   similar gene expression. Shared nearest neighbor graph-based clustering was repeated

760   several times using Seurat package's FindNeighbors and FindClusters functions with a

761   resolution ranging from 1 to 7.

762   From these three different cell states, the following information was quantified:

763   • p($B_{sig}|Exp_{eng}$): For each Experimental_engagement_state we quantified the probability

764   distribution of each Behavioral_signature (**Figure 4F**. This was achieved by

765   reproducing the Experimental_engagement_states *in silico* on our imaging data. These

766   values were calculated separately for CD4$^+$ and CD8$^+$ TEGs.

767   • p($Exp_{eng}|U_{cl}$): For each UMAP_cluster, we quantified the probability of each

768   Experimental_engagement_state to belong to this cluster.

769   Given these probabilities, we then quantified for each T cell the probability distribution of each

770   unique Behavioral_signature in each UMAP_cluster, using the equation:

771

772   As a result, each cell was assigned a certain probability distribution for different behavioral

773   signatures. To refine the probability map, the same process was repeated for 7 runs with

774   different cluster sizes and the final probability distributions were averaged per cell. Note that

775   for cells belonging to the *No target control* Experimental_engagement_state, a

776   Behavioral_signature called *No target control* was assumed. The probability distribution along

777 the pseudotime trajectory was plotted using pheatmap package[70] of scaled values for each

778 behavioral signature. Given that the non-engaged behavioral signatures (*Static, Lazy, Slow*

779 *scanner, Medium scanner, Super scanner*) exhibited an identical probability map, their values

780 were plotted together. For visualization purpose, extreme outlier values of skewed distributions

781 were transformed to a maximal cutoff value. Based on the probability distribution of different

782 behavioral signatures, the pseudotime was divided into 4 stages (Baseline (no organoids);

783 Environmental stimuli, Short engagement, Prolonged engagement) for each TEG subtype

784 (CD8^{+eff}, CD4^{+eff} and CD4^{+mem}).

785

786 Differential gene expression analysis of TEGs co-cultured with distinct PDO cultures

787 For comparison of TEGs targeting 10T or 13T PDOs (**Figures 5A-5C**), SORTseq dataset was

788 used including TEGs from distinct Experimental engagement states: *Non-engaged^{Enriched}* and

789 *super engager*. *No target control* TEGs were used as a control group. SORTseq data were

790 mapped and quantified and visualized with UMAP as described above. Differential gene

791 expression analysis was performed with the FindMarkers function from Seurat v3. Common

792 and specific gene sets were filtered and visualized by Venn diagram with the VennDiagram

793 package.

794

795 Gene set enrichment analysis

796 The functional enrichment analysis in this study for pathway and biological processes

797 annotations for gene sets of interest was conducted using ToppFun on the ToppGene

798 Suite(Kaimal et al.) (**Figures 1H, S4C, and S5B**). An enrichment score was assigned based on

799 gene enrichment ratio and log p value. For redundant annotations, the annotation with the

800 highest gene enrichment ratio was selected. The pathways and biological processes with

801 highest enrichment for gene set of interest were displayed in RStudio.

Serial killer gene signature analysis

Genes of CL7 (**Figure 4G; Table S4 and S5**) were analysed to identify a unique signature for killer TEGs. 61/83 genes composing this cluster were common to TEGs incubated with 13T and 10T organoids and underwent extensive literature curation to identify genes with a known role in T cell cytotoxicity; T cell biology (not related to cytotoxicity); morphological plasticity or other processes such as GTPase signaling, ribogenesis and transcriptional regulation. Overlapping gene roles were plotted in a Venn diagram with the Venneuler package (**Figure 4K**).

Statistical analysis

Statistical analysis was performed using R or Prism 7 software (GraphPad). Results are represented as mean ± s.e.m. unless indicated otherwise; *n* represents independent biological replicates. Two-tailed unpaired t-tests were performed between two groups, unless indicated otherwise. Pearson correlation was used for paired comparison between three different readouts (IFN-γ production, cell viability and live imaging). For live-cell imaging, the increase in dead cell dye between the first and last time point was used as measure. To compare tumor volume in mice treated with TEGs or TEG001 mock cells, two-way ANOVA with repeated measures was performed. To compare frequencies of different behavioral signatures between PDOs, a Pearson's Chi-squared test was applied. To compare the percentage of dead organoids when TEGs were co-cultured with different PDOs, a one-way ANOVA followed by Bonferroni correction was performed. To estimate the change in correlation between 13T PDO death dynamics and cumulative contact with TEGs for different behavioral signatures, data was fitted to a linear mixed model with experimental replicate as random effect to account for variation between them. For cell type enrichment analysis of TEGs' first and second action after engagement, a hypergeometric test was used (Fisher exact test). For comparisons of

827   percentages of distinct TEG subtypes in the same well ($CD4^+$ vs $CD8^+$ or $NCAM^+$ vs NCAM),

828   for each behavioral signature data were fitted to a linear regression model with each individual

829   replicate set as random effect to account for variation between them. For each fitted model, an

830   analysis of variance was computed with an F-test. For comparison of IFN-β treatment, paired

831   t test was performed.

832

833   **Data availability**

834   RNA sequencing and imaging data is available upon request.

835

836   **Code availability**

837   Upon request.

838

863

Author contributions

865   J.F.D grew organoids and performed imaging experiments with assistance from H.G.R., E.J.V.

866 and M.G. M.A. designed and performed the computational analysis. M.A. and J.F.D. analyzed

867 the data. M.B.B. and M.B.R. assisted with imaging data processing. J.F.D., A.K.L.W. and E.K.

868 performed scRNAseq experiments. J.P. and D.F. processed PDO sequencing data. H.C.R.A.

869 performed NCAM1 sorts. F.K. and P.B. analyzed the scRNAseq data. A.C. and E.K. produced

870 TEGs and performed IFN-γ assays. H.G.R., I.J. and A.D.M. performed *in vivo* experiments.

871 A.M.B assisted with computational analysis. R.L.I and M.B.R. made the video. O.K. provided

872 organoid cultures. Y.B.E. and K.K. provided support and developed the co-culture live cell

873 staining protocol that was used and further adapted. J.F.D, M.A. and A.C.R. designed the study

874 and wrote the manuscript with support from A.M.M.E., E.J.W., H.G.S, Z.S., J.K. and H.C.

875 This work was jointly supervised by A.C.R, Z.S, J.K, H.C who share senior authorship.

876

877   **Declaration of Interests**

878   H.C., Y.B.E. and K.K. are named as inventors on patents or patents pending on Lgr5-stem cell

879   based organoid technology and immune cell organoid co-cultures. For full disclosure of HC:

880   https://www.uu.nl/staff/JCClevers/Additional%20functions. J.F.D. is named as inventor on a

881   patent related to organoid technology. Z. S. and J.K are inventors on different patents with γδ

882   TCR sequences, recognition mechanisms, and isolation strategies. J.K. receives research

883   funding from and is scientific advisor and shareholder of Gadeta (www.gadeta.nl).

884

885   **Figure legends**

886

887   **Figure 1. TEG efficacy across organoids of multiple breast cancer subtypes detected by**

888   **multispectral 3D live imaging and *in vivo* TEG targeting**. (**A**) Schematic representation of

889   co-culture preparation. TEGs were generated by engineering peripheral blood αβ T cells to

890   express a defined Vγ9/Vδ2 TCR via retroviral transduction. TEGs were then co-cultured with

891   patient-derived breast organoids (PDOs). (**B**) Schematic representation of the BEHAV3D

892   platform. Fluorescent dyes were combined to specifically label organoids (yellow), TEGs

893   (blue) and dead cells (red). Co-cultures of organoids and TEGs were imaged in 96-well plates

894   using spectral confocal microscopy in 3D, followed by segmentation and tracking of organoids

895   and T cells, and subsequent behavior classification. TEGs of experimental conditions as

896   indicated were sequenced and pseudotime ordering was used to integrate behavioral data.

897   Identified targets were used to manipulate TEG targeting. (**C**) Representative 3D multispectral

898   images of breast PDO cultures (yellow) that show low (1837M), intermediate (10T) and high

899   (13T) killing by TEGs (blue) at the indicated time points of imaging. Dead cells depicted in

900   red. Scale bars, 100 μm (left two columns) and 30 μm (right two columns). (**D**) Quantification

901   of killing of organoids derived from 14 different BC patients upon 24 hr co-culture with TEGs

902   by 3D live cell imaging. All data were corrected for control LM1 T cell responses. (n = 4

903   independent experiments; mean ± s.e.m.; TNBC = triple negative breast cancer; ER = estrogen

904   receptor; PR = progesterone receptor). (**E**) Representative 3D multispectral images showing

905   automated rendering of single organoids (confetti colors) and T cells (blue) (left image), and

906   an enlarged section showing presence of dead cell dye (red) in a single organoid (transparent

907   purple rendering) and TEGs (transparent blue rendering) at the indicated time of co-culture.

908   Scale bars, 100 μm (left image) and 30 μm (right image). (**F**) Quantification of the percentage

909   of dying single organoids (% of total) over time for each PDO co-cultured with TEGs (n = 4

910   independent experiments; mean ± s.e.m.). (**G**) Quantification of the volume of tumors overtime

911   generated by subcutaneous transplantation of 13T (black lines) or 169M organoids (orange

912   lines). Animals received 2 injections of either TEGs (dashed line) or control TEG011 cells

913   (Control; solid line) at the indicated timepoints. (n ≥5 per condition; mean ± s.e.m.). Statistical

914   analysis was performed by Two-Way ANOVA with repeated measures: 13T-TEG vs 13T-

915   control p < 0.0001; 169M-TEG vs 169M-control p=0.0016. (**H**) Gene ontology enrichment

916   analysis of differentially expressed genes between the six highest versus six lowest TEG-

917   sensitive organoid cultures from d.

918

919   **Figure 2. TEGs exposed to PDOs display high diversities in their behavior with distinct**

920   **killing potential.** (**A**) Representative image of automated tracking of each TEG (left image;

921   10 hrs tracks are rainbow-colored for time). Tracks were classified according to TEG behavior

922   and back-projected in the image (right image; color-coded by cluster). Scale bars, 50 μm. (**B**)

923   Umap plot showing nine color-coded clusters identified by unbiased multivariate timeseries

924   dynamic time warping analysis. Each data point represents a T cell track of 3.3 hrs. Numbers

925   refer to cluster names presented in (C). (**C**) Heatmap depicting relative values of T cell features

926   indicated for each cluster, named according to their most distinct characteristics. AU: arbitrary

927   units in respect to maximal and minimal values for each feature. (OC, organoid contact; Dis,

928   square displacement; Sp, speed; TI, T cell interactions; CD, cell death) (**D**) 3D-rendered images

929   of 100T (low-targeting; left image) and 13T (high-targeting; right image) organoids (grey) and

930   TEGs with 3.3 hr tracks belonging to *lazy* (green) and *super engager* (red) clusters. Scale bars,

931   20 μm. (**E**) Behavioral cluster distribution of TEGs co-cultured with the indicated PDOs and a

932   normal organoid culture (left plot), in relation to their killing capacity (right bar graph)

933   represented as the percentage of dying organoids (% of total) (n ≥ 3 independent experiments;

934   mean ± s.e.m.). X^2 test; p = 1.132e-08. (**F**) Pearson correlation between behavior cluster size

935   and the percentage of dying organoids represented in d. CL9 p=0.00006; CL8 p= 0.009; CL7

936   p=0.006; CL5 p=0.014; CL4 p=0.022; CL2 p=0.0019. (n ≥ 3 independent experiments; mean).

937   (**G**) Change in correlation between 13T organoid death dynamics (measured as increase in dead

938   cell dye) and cumulative contact with TEGs (from cluster (C)7-9). Data is represented as mean

939   correlation per timepoint of all single organoids (n = 4 independent experiments). Linear mixed

940   model fitting with each experimental replicate as a random effect: C9 vs C8 p= 5.19e-06; C9

941   vs C7 p < 2e-16.

942

943   **Figure 3. Unique targeting features of TEGs subpopulations and serial killer potential**.

944   (**A**) Representative 3D-rendered images of CD4$^+$ (blue) and CD8$^+$ (red) TEGs and their full

945   tracks (up to 10 hrs) co-cultured with the 13T organoids (grey surface rendering at t = 0).

946   Overview: Scale bar, 50 μm. Zoomed images: Scale bar, 30 μm (**B**) Relative behavioral cluster

947   distribution of TEGs co-cultured with the indicated PDOs and a normal organoid culture. (**C**)

948   Behavioral cluster size difference (%) between CD4$^+$ and CD8$^+$ TEGs co-cultured with the

949   indicated PDOs and a normal organoid culture calculated from B. (n ≥ 3 independent

950   experiments for each co-culture; mean ± s.e.m.) Linear regression model fitting with each well

951   as a random effect: C9 p=7.52E-06; C8 p=0.0034; C7 p=0.00018; C6 p=0.000023; C5

952   p=0.0062; C4 p=0.01; C3 p= 0.001; C1 p=3.01E-06. (**D**) Quantification of the first action and

953   second action of CD4$^+$ and CD8$^+$ TEGs after they engaged with an organoid. n = 3 replicates.

954   Hypergeometric test was used to analyze cell type enrichment in each category. "Kills multiple

955   cells" p<0.0001; "Kills one cell" p= 0.000015; "No killing" p= 0.0018. (**E**) 3D multispectral

956   images showing a CD4$^+$ TEG (green) that kills a 13T tumor cell (becomes red) in a first

957   organoid (yellow) and a second tumor cell in a neighboring organoid (upper panel), and a CD8$^+$

958   TEG (blue) killing a complete 13T organoid of ~18 cells (yellow becoming red) in 11 hrs

959   (lower panel). Scale bars, 30 μm. (**F**) Processed images of j showing 3D-rendered organoids

960 (grey) at t = 0 and the CD4$^+$ TEG (green) or the CD8$^+$ TEG (blue) with their full track rainbow-

961 colored for time. Scale bars, 10 μm. (**G**) Quantification of the number of cells killed in a

962 sequence by CD8$^+$ TEGs in time. (n = 3 independent experiments). (**H**) Quantification of the

963 time it takes to kill one 13T tumor cell for CD4$^+$ TEGs and CD8$^+$ TEGs (n = 3 independent

964 experiments). (**I**) UMAP embedding showing the expression levels of NCAM1. Color gradient

965 represents the log$_2$-transformed normalized counts of genes. (**J**) Quantification of the

966 percentage of dying 13T organoids (% of total) at 10 hrs of co-culture with either sorted

967 NCAM1$^-$CD8$^+$ TEGs or NCAM1$^+$CD8$^+$ TEGs (n = 5 independent experiments; mean ± s.e.m.).

968 Two-tailed unpaired t test, p= 0.0001036. (**K**) Schematic representation of fluorescent labeling

969 strategy of CD8$^+$ TEGs with NCAM1 nanobody and efluor-450 to image and track NCAM1-

970 positive versus -negative TEGs. (**L**) Behavioral cluster difference (%) between NCAM1$^-$CD8$^+$

971 TEGs or NCAM1$^+$CD8$^+$ TEGs co-cultured with 13T organoids. (n = 6 independent

972 experiments; mean ± s.e.m.). Linear regression model fitting with each experimental replicate

973 as a random effect: CL9 p=0.0002; CL8 p=0.07; CL2 p=0.005; CL1 p=0.02. (**M**) 3D-rendered

974 images of 13T organoids (grey) from the same well with NCAM+ 'super-engager' CD8+ TEGs

975 (top image) and NCAM- 'lazy' and 'dying' CD8+ TEGs (bottom image). Scale bars, 10 μm.

976

977 **Figure 4. Behavioral-transcriptomic profiling of TEGs upon PDO exposure, engagement**

978 **and killing.** (**A**) Schematic representation of cell population separation for isolation and

979 sequencing of *super-engaged*, *engaged*, *non-engaged*; *non-engaged^{Enriched}*, and *no target*

980 *control* TEGs. (**B**) Distribution of the 9 behavioral signatures described in **Figures 2B and 2C**

981 of the indicated behavior-enriched TEG populations isolated at 6 hrs of co-culture. (**C-E**)

982 UMAP embedding of pooled scRNAseq profiles showing distribution of, CD8^{+eff}, CD4^{+eff},

983 CD4^{+mem} TEGs (C), the 5 behavior-enriched TEG populations described in a (D), and

984 normalized gene expression of IFNG and GZMB (E). Colors represent the log$_2$-transformed

985   normalized counts of genes. (**F**) Heatmap representing the probability distribution of different

986   behavioral signatures and *no target control* over pseudotime for CD8^{+eff}, CD4^{+eff} and CD4^{+mem}

987   TEGs. Color represents the scaled probability for each behavioral group. (**G**) Heatmap

988   showing normalized gene expression dynamics of TEGs upon exposure and engagement to

989   13T PDOs. Columns represent T cells ordered in pseudotime, rows represent the expression of

990   genes, grouped based on similarity, resulting in 8 gene clusters (CL). CL1-3 represent gene

991   expression patterns shared among TEG subsets. CL4-8 show different expression dynamics

992   between TEG subsets. Horizontal color-bar (on top) represents the corresponding stage of

993   targeting based on data in f. (**H**) Averaged gene expression over pseudotime for all genes from

994   indicated GO terms for the indicated TEG subtypes. Graph background color-shading represent

995   the corresponding stage of targeting. Line colors indicate GO term. (**I**) Gene-expression dot

996   plot for a curated subset of genes at different stages of targeting. Rows depict genes. Dot color

997   gradient indicates average expression, while size reflects the proportion of cells expressing a

998   particular gene (%). (**J**) Violin plots for different TEG subtypes showing averaged expression

999   of genes related to GO term 'Regulation of cell killing' enriched in CL7 from g. Colors indicate

1000   different stages of targeting. (**K**) Venn diagram depicting common and unique functions from

1001   61 conserved genes composing a (serial) killer gene signature.

1002

1003   **Figure 5. IFN-I signaling in PDOs primes TEG efficacy.** (**A**) Top panel: UMAP embedding

1004   of pooled scRNA-seq profiles from *super-engaged* and *non-engaged*^{Enriched} TEG populations

1005   co-cultured with either 13T or 10T PDOs; and *no target control* T cells. TEGs are colored per

1006   experimental condition. Bottom panel: UMAP plot showing the expression levels of IFNG and

1007   GZMB. Colors represent the log$_2$-transformed normalized counts of genes. (**B**) Venn diagrams

1008   depicting common and unique genes upregulated in TEGs upon 13T and 10T organoid

1009   exposure (environmental stimuli; top panel) or prolonged engagement (*super engagers*; bottom

1010 panel). (**C**) Heatmap of gene expression for genes involved in functional annotations of interest

1011 ("Response to IFN-I", "Cytokine response"), grouped according to TEG populations. (**D**)

1012 IFNA and IFNB expression in PDOs from the BC panel in **Figure 1D**. (**E-G**) Quantification

1013 of dying single organoids in presence or absence of recombinant IFN-β for the following

1014 conditions: organoids co-cultured with TEGs with direct addition of IFN-β, corrected for

1015 responses of LM1 control T cells (E); organoids pre-incubated with IFN-β for 24 hrs before

1016 co-culture with TEGs, corrected for responses of LM1 control T cells (F), and organoids pre-

1017 incubated with IFN-β for 24 hrs and cultured in absence of TEGs (G). Lines connect

1018 experimental replicates. (n≥3). Statistical analysis in (F) was performed by paired t test: 34T-

1019 IFN-β vs 34T-control p < 0.0006; 27T-IFN-β vs 27T-control p < 0.0216; 10T-IFN-β vs 10T-

1020 control p < 0.0402.

1021

1022 **References**

1023 Abbas, A., et al. (2020). The activation trajectory of plasmacytoid dendritic cells in vivo during

1024 a viral infection. Nature Immunology *21*, 983–997.

1025 Ali, M., Jones, M.W., Xie, X. et al. (2019). TimeCluster: dimension reduction applied to

1026 temporal data for visual analytics. Vis Comput *35*, 1013–1026.

1027 Asmal, M., Colgan, J., Naef, F., Yu, B., Lee, Y., Magnasco, M., and Luban, J. (2003).

1028 Production of ribosome components in effector CD4+ T cells is accelerated by TCR

1029 stimulation and coordinated by ERK-MAPK. Immunity *19*, 535–548.

1030 Bar-Ephraim, Y.E., Kretzschmar, K., and Clevers, H. (2019). Organoids in immunological

1031 research. Nat Rev Immunol *28*, 514.

1032 Barnes, S.E., Wang, Y., Chen, L., Molinero, L.L., Gajewski, T.F., Evaristo, C., and Alegre,

1033 M.-L. (2015). T cell-NF-κB activation is required for tumor control in vivo. J Immunother

1034 Cancer *3*, 1.

1035 Becht, E., McInnes, L., Healy, J., Dutertre, C.-A., Kwok, I.W.H., Ng, L.G., Ginhoux, F., and

1036 Newell, E.W. (2019). Dimensionality reduction for visualizing single-cell data using UMAP.

1037 Nat. Biotechnol *37*, 34-44.

1038 Benci, J.L., Xu, B., Qiu, Y., Wu, T.J., Dada, H., Twyman-Saint Victor, C., Cucolo, L., Lee,

1039 D.S.M., Pauken, K.E., Huang, A.C., et al. (2016). Tumor Interferon Signaling Regulates a

1040 Multigenic Resistance Program to Immune Checkpoint Blockade. Cell *167*, 1540–1554.e12.

1041 Borden, E.C. (2019). Interferons α and β in cancer: therapeutic opportunities from new insights.

1042 Nat Rev Drug Discov *18*, 219–234.

1043 Boukhaled, G.M., Harding, S., and Brooks, D.G. (2021). Opposing Roles of Type I Interferons

1044 in Cancer Immunity. Annu Rev Pathol *16*, 167–198.

1045 Breiman, L. (2001). Random Forests. Machine Learning *45*, 5–32.

1046 Broutier, L., Andersson-Rolf, A., Hindley, C.J., Boj, S.F., Clevers, H., Koo, B.-K., and Huch,

1047 M. (2016). Culture and establishment of self-renewing human and mouse adult liver and

1048 pancreas 3D organoids and their genetic manipulation. Nat Protoc *11*, 1724–1743.

1049 Burke, M.K., Dunham, J.P., Shahrestani, P., Thornton, K.R., Rose, M.R., Long A.D. (2010)

1050 Genome-wide analysis of a long-term evolution experiment with Drosophila. Nature *467*, 587-

1051 90.

1052 Cai, Y., Hossain, M.J., Hériché, J.-K., Politi, A.Z., Walther, N., Koch, B., Wachsmuth, M.,

1053 Nijmeijer, B., Kueblbeck, M., Martinic-Kavur, M., et al. (2018). Experimental and

1054   computational framework for a dynamic protein atlas of human cell division. Nature *561*, 411–

1055   415.

1056   Candelli, T. et al. (2018) Sharq, a versatile preprocessing and QC pipeline for Single Cell RNA-

1057   seq. BioRxiv 250811

1058   Cao, J., Spielmann, M., Qiu, X. et al. (2019). The single-cell transcriptional landscape of

1059   mammalian organogenesis. Nature *566*, 469-502.

1060   Cao, Y. et al. (2020) SCSA: a cell type annotation tool for single-cell RNA-seq data. Frontiers

1061   in Genetics *11*, 490.

1062   Cattaneo, C.M., Dijkstra, K.K., Fanchi, L.F., Kelderman, S., Kaing, S., van Rooij, N., Van den

1063   Brink, S., Schumacher, T.N., and Voest, E.E. (2020). Tumor organoid-T-cell coculture

1064   systems. Nat Protoc *15*, 15–39.

1065   Cazaux, M., Grandjean, C.L., Lemaître, F., Garcia, Z., Beck, R.J., Milo, I., Postat, J., Beltman,

1066   J.B., Cheadle, E.J., and Bousso, P. (2019). Single-cell imaging of CAR T cell activity in vivo

1067   reveals extensive functional and anatomical heterogeneity. J. Exp. Med. *216*, 1038–1049.

1068   Chen, D.S., and Mellman, I. (2017). Elements of cancer immunity and the cancer-immune set

1069   point. Nature *541*, 321–330.

1070   Collins, S., Wolfraim, L.A., Drake, C.G., Horton, M.R., and Powell, J.D. (2006). Cutting Edge:

1071   TCR-induced NAB2 enhances T cell function by coactivating IL-2 transcription. The Journal

1072   of Immunology *177*, 8301–8305.

1073   Crowther, M.D., et al. (2020). Genome-wide CRISPR-Cas9 screening reveals ubiquitous T cell

1074   cancer targeting via the monomorphic MHC class I-related protein MR1. Nature Immunology

1075   *21*, 178–185.

1076   Dekkers, J.F., et al. (2019). High-resolution 3D imaging of fixed and cleared organoids. Nat

1077   Protoc *14*, 1756–1771.

1078   Dekkers, J.F., et al. (2021). Long-term culture, genetic manipulation and xenotransplantation

1079   of human normal and breast cancer organoids. Nat Protoc *16*, 1936-1965.

1080   Dijkstra K.K. et al. (2018). Generation of Tumor-Reactive T Cells by Co-culture of Peripheral

1081   Blood Lymphocytes and Tumor Organoids. Cell *174*, 1586–1598.e12.

1082   Dunn, G.P., et al. (2005). A critical function for type I interferons in cancer immunoediting.

1083   Nature Immunology *6*, 722–729.

1084   Esteva, F.J., Hubbard-Lucey, V.M., Tang, J., and Pusztai, L. (2019). Immunotherapy and

1085   targeted therapy combinations in metastatic breast cancer. Lancet Oncol. *20*, e175–e186.

1086   Ganesh, K., Wu, C., O'Rourke, K.P., Szeglin, B.C., Zheng, Y., Sauvé, C.-E.G., Adileh, M.,

1087   Wasserman, I., Marco, M.R., Kim, A.S., et al. (2019). A rectal cancer organoid platform to

1088   study individual responses to chemoradiation. Nat. Med. *25*, 1607–1614.

1089   Gründer, C., van Dorp, S., Hol, S., Drent, E., Straetemans, T., Heijhuurs, S., Scholten, K.,

1090   Scheper, W., Sebestyen, Z., Martens, A., et al. (2012). γ9 and δ2CDR3 domains regulate

1091   functional avidity of T cells harboring γ9δ2TCRs. Blood *120*, 5153–5162.

1092   Hafemeister, C., and Satija, R. (2019). Normalization and variance stabilization of single-cell

1093   RNA-seq data using regularized negative binomial regression. Genome Biol. *20*, 296.

1094   Halle, S., Keyser, K.A., Stahl, F.R., Busche, A., Marquardt, A., Zheng, X., Galla, M.,

1095   Heissmeyer, V., Heller, K., Boelter, J., et al. (2016). In Vivo Killing Capacity of Cytotoxic T

1096   Cells Is Limited and Involves Dynamic Interactions and T Cell Cooperativity. Immunity *44*,

1097   233–245.

1098   Jacob, F., Salinas, R.D., Zhang, D.Y., Nguyen, P.T.T., Schnoll, J.G., Wong, S.Z.H., Thokala,

1099   R., Sheikh, S., Saxena, D., Prokop, S., et al. (2020). A Patient-Derived Glioblastoma Organoid

1100   Model and Biobank Recapitulates Inter- and Intra-tumoral Heterogeneity. Cell *180*, 188–

1101   204.e22.

1102   Jacquelot, N., Yamazaki, T., Roberti, M.P., Duong, C.P.M., Andrews, M.C., Verlingue, L.,

1103   Ferrere, G., Becharef, S., Vétizou, M., Daillère, R., et al. (2019). Sustained Type I interferon

1104   signaling as a mechanism of resistance to PD-1 blockade. Cell Res *29*, 846–861.

1105   Johanna, I., Straetemans, T., Heijhuurs, S., Aarts-Riemens, T., Norell, H., Bongiovanni, L., de

1106   Bruin, A., Sebestyen, Z., and Kuball, J. (2019). Evaluating in vivo efficacy - toxicity profile of

1107   TEG001 in humanized mice xenografts against primary human AML disease and healthy

1108   hematopoietic cells. J Immunother Cancer *7*, 69.

1109   June, C.H., and Sadelain, M. (2018). Chimeric Antigen Receptor Therapy. N Engl J Med *379*,

1110   64–73.

1111   Kaimal V, Bardes EE, Tabar SC, Jegga AG, Aronow BJ. (2010). ToppCluster: a multiple gene

1112   list feature analyzer for comparative enrichment clustering and network-based dissection of

1113   biological systems. Nucleic Acids Res, *38* (Web Server issue):W96-W102.

1114   Kierkels, G.J.J., Scheper, W., Meringa, A.D., Johanna, I., Beringer, D.X., Janssen, A.,

1115   Schiffler, M., Aarts-Riemens, T., Kramer, L., Straetemans, T., et al. (2019). Identification of a

1116   tumor-specific allo-HLA-restricted γδTCR. Blood Adv *3*, 2870–2882.

1117   Kolde, R., et al. (2015). Package "pheatmap." Mran.Microsoft.com

1118   Liu, H., Rhodes, M., Wiest, D.L., and Vignali, D.A. (2000). On the dynamics of TCR:CD3

1119   complex cell surface expression and downmodulation. Immunity *13*, 665–675.

1120 Lukonin, I., Serra, D., Meylan, L.C., Volkmann, K., Baaten, J., Zhao, R., Meeusen, S., Colman,

1121 K., Maurer, F., Stadler, M.B., et al. (2020). Phenotypic landscape of intestinal organoid

1122 regeneration. Nature *586*, 275–280.

1123 Marcu-Malina, V., Heijhuurs, S., van Buuren, M., Hartkamp, L., Strand, S., Sebestyen, Z.,

1124 Scholten, K., Martens, A., and Kuball, J. (2011). Redirecting αβ T cells against cancer cells by

1125 transfer of a broadly tumor-reactive γδT-cell receptor. Blood *118*, 50–59.

1126 McInnes, L., Healy, J., Melville J. (2020) Umap: Uniform manifold approximation and

1127 projection for dimension reduction. ArXiv 1802.03426

1128 Muraro, M.J., Dharmadhikari, G., Grün, D., Groen, N., Dielen, T., Jansen, E., van Gurp, L.,

1129 Engelse, M.A., Carlotti, F., de Koning, E.J.P., et al. (2016). A Single-Cell Transcriptome Atlas

1130 of the Human Pancreas. Cell Syst *3*, 385–394.e3.

1131 Neal, J.T., et al. (2018). Organoid Modeling of the Tumor Immune Microenvironment. Cell

1132 *175*, 1972–1988.e16.

1133 Ooft, S.N., Weeber, F., Dijkstra, K.K., McLean, C.M., Kaing, S., van Werkhoven, E., Schipper,

1134 L., Hoes, L., Vis, D.J., van de Haar, J., et al. (2019). Patient-derived organoids can predict

1135 response to chemotherapy in metastatic colorectal cancer patients. Sci Transl Med *11*.

1136 Preti, M.G., Bolton, T., Van De Ville, D., (2017). The dynamic functional connectome: State-

1137 of-the-art and perspectives. Neuroimage, *160*:41-54.

1138 Rigau, M., Ostrouska, S., Fulford, T.S., Johnson, D.N., Woods, K., Ruan, Z., McWilliam,

1139 H.E.G., Hudson, C., Tutuka, C., Wheatley, A.K., et al. (2020). Butyrophilin 2A1 is essential

1140 for phosphoantigen reactivity by γδ T cells. Science *367*.

1141 Rios, A.C., Clevers, H. (2018) Imaging organoids: a bright future ahead. Nat Methods *15*, 24-
1142 26

1143 Sachs, N., et al. (2018). A Living Biobank of Breast Cancer Organoids Captures Disease
1144 Heterogeneity. Cell *172*, 373-368.e10

1145 Schafer, S.T., Paquola, A.C.M., Stern, S., Gosselin, D., Ku, M., Pena, M., Kuret, T.J.M.,
1146 Liyanage, M., Mansour, A.A., Jaeger, B.N., et al. (2019). Pathological priming causes
1147 developmental gene network heterochronicity in autistic subject-derived neurons. Nat
1148 Neurosci *22*, 243–255.

1149 Scheper, W., Gründer, C., Straetemans, T., Sebestyen, Z., and Kuball, J. (2013). Hunting for
1150 clinical translation with innate-like immune cells and their receptors. Leukemia *28*, 1181–1190.

1151 Schnalzger, T.E., de Groot, M.H., Zhang, C., Mosa, M.H., Michels, B.E., Röder, J., Darvishi,
1152 T., Wels, W.S., and Farin, H.F. (2019). 3D model for CAR-mediated cytotoxicity using patient-
1153 derived colorectal cancer organoids. Embo J. *38*, e100928.

1154 Schumacher, T.N., Scheper, W., and Kvistborg, P. (2019). Cancer Neoantigens. Annu Rev
1155 Immunol *37*, 173–200.

1156 Sebestyen, Z., Prinz, I., Déchanet-Merville, J., Silva-Santos, B., and Kuball, J. (2019).
1157 Translating gammadelta (γδ) T cells and their receptors into cancer cell therapies. Nat Rev
1158 Drug Discov *32*, 1–16.

1159 Serra, D., Mayr, U., Boni, A., Lukonin, I., Rempfler, M., Challet Meylan, L., Stadler, M.B.,
1160 Strnad, P., Papasaikas, P., Vischi, D., et al. (2019). Self-organization and symmetry breaking
1161 in intestinal organoid development. Nature *569*, 66–72.

1162   Sistigu, A., Yamazaki, T., Vacchelli, E., Chaba, K., Enot, D.P., Adam, J., Vitale, I., Goubar,

1163   A., Baracco, E.E., Remédios, C., et al. (2014). Cancer cell-autonomous contribution of type I

1164   interferon signaling to the efficacy of chemotherapy. Nat. Med. *20*, 1301–1309.

1165   Straetemans, T., Gründer, C., Heijhuurs, S., Hol, S., Slaper-Cortenbach, I., Bönig, H.,

1166   Sebestyen, Z., and Kuball, J. (2015). Untouched GMP-Ready Purified Engineered Immune

1167   Cells to Treat Cancer. Clin. Cancer Res. *21*, 3957–3968.

1168   Straetemans, T., Kierkels, G.J.J., Doorn, R., Jansen, K., Heijhuurs, S., Santos, Dos, J.M., van

1169   Muyden, A.D.D., Vie, H., Clemenceau, B., Raymakers, R., et al. (2018). GMP-Grade

1170   Manufacturing of T Cells Engineered to Express a Defined γδTCR. Front. Immunol. *9*, 1062.

1171   Stuart, T., Butler, A., Hoffman, P., Hafemeister, C., Papalexi, E., Mauck, W.M., Hao, Y.,

1172   Stoeckius, M., Smibert, P., and Satija, R. (2019). Comprehensive Integration of Single-Cell

1173   Data. Cell *177*, 1888–1902.e21.

1174   Szabo, P.A., Levitin, H.M., Miron, M., Snyder, M.E., Senda, T., Yuan, J., Cheng, Y.L., Bush,

1175   E.C., Dogra, P., Thapa, P., et al. (2019). Single-cell transcriptomics of human T cells reveals

1176   tissue and activation signatures in health and disease. Nat Commun *10*, 4706–4716.

1177   Tan, T.C.J., Knight, J., Sbarrato, T., Dudek, K., Willis, A.E., and Zamoyska, R. (2017).

1178   Suboptimal T-cell receptor signaling compromises protein translation, ribosome biogenesis,

1179   and proliferation of mouse CD8 T cells. Proc. Natl. Acad. Sci. U.S.A. *114*, E6117–E6126.

1180   Terrier, B., Bièche, I., Maisonobe, T., Laurendeau, I., Rosenzwajg, M., Kahn, J.-E., Diemert,

1181   M.-C., Musset, L., Vidaud, M., Sène, D., et al. (2010). Interleukin-25: a cytokine linking

1182   eosinophils and adaptive immunity in Churg-Strauss syndrome. Blood *116*, 4523–4531.

1183   Tiriac, H., Belleau, P., Engle, D.D., Plenker, D., Deschênes, A., Somerville, T.D.D., Froeling,

1184   F.E.M., Burkhart, R.A., Denroche, R.E., Jang, G.-H., et al. (2018). Organoid Profiling

1185   Identifies Common Responders to Chemotherapy in Pancreatic Cancer. Cancer Discov *8*,

1186   1112–1129.

1187   Tuveson, D., Clevers, H. (2019) Cancer modeling meets human organoid technology. Science

1188   *364*, 952-955.

1189   Van Acker, H.H., Capsomidis, A., Smits, E.L., and Van Tendeloo, V.F. (2017). CD56 in the

1190   Immune System: More Than a Marker for Cytotoxicity? Front. Immunol. *8*, 892.

1191   Van der Leun, A.M., Thommen, D.S., and Schumacher, T.N. (2020). CD8+ T cell states in

1192   human cancer: insights from single-cell analysis. Nat. Rev. Cancer *20*, 218–232.

1193   Van Ineveld et al. mLSR-3D and STAPL-3D reveals the spatio-phenotypic patterning of cells

1194   in healthy and tumor tissues. Nat. Biotechnol, *in press*.

1195   Vlachogiannis, G., Hedayat, S., Vatsiou, A., Jamin, Y., Fernández-Mateos, J., Khan, K.,

1196   Lampis, A., Eason, K., Huntingford, I., Burke, R., et al. (2018). Patient-derived organoids

1197   model treatment response of metastatic gastrointestinal cancers. Science *359*, 920–926.

1198   Vyborova, A., et al. (2020). γ9δ2T cell diversity and the receptor interface with tumor cells. J.

1199   Clin. Invest. *130*, 4637-4651

1200   Weigelin, B., et al. (2020) Cancer cell elimination by cytotoxic T cell cooperation and additive

1201   damage. BioRxiv 2020.04.22.054718

1202   Wilkinson, L. (2011). ggplot2: elegant graphics for data analysis by WICKHAM, H.

1203   doi:10.1111/j.1541-0420.2011.01616.x

1204   Yamamoto, T.N., Kishton, R.J., and Restifo, N.P. (2019). Developing neoantigen-targeted T

1205   cell-based treatments for solid tumors. Nat. Med. *25*, 1488–1499.

1206   Yao, Y., Xu, X., Yang, L., Zhu, J., Wan, J., Shen, L., Xia, F., Fu, G., Deng, Y., Pan, M., et al.

1207   (2020). Patient-Derived Organoids Predict Chemoradiation Responses of Locally Advanced
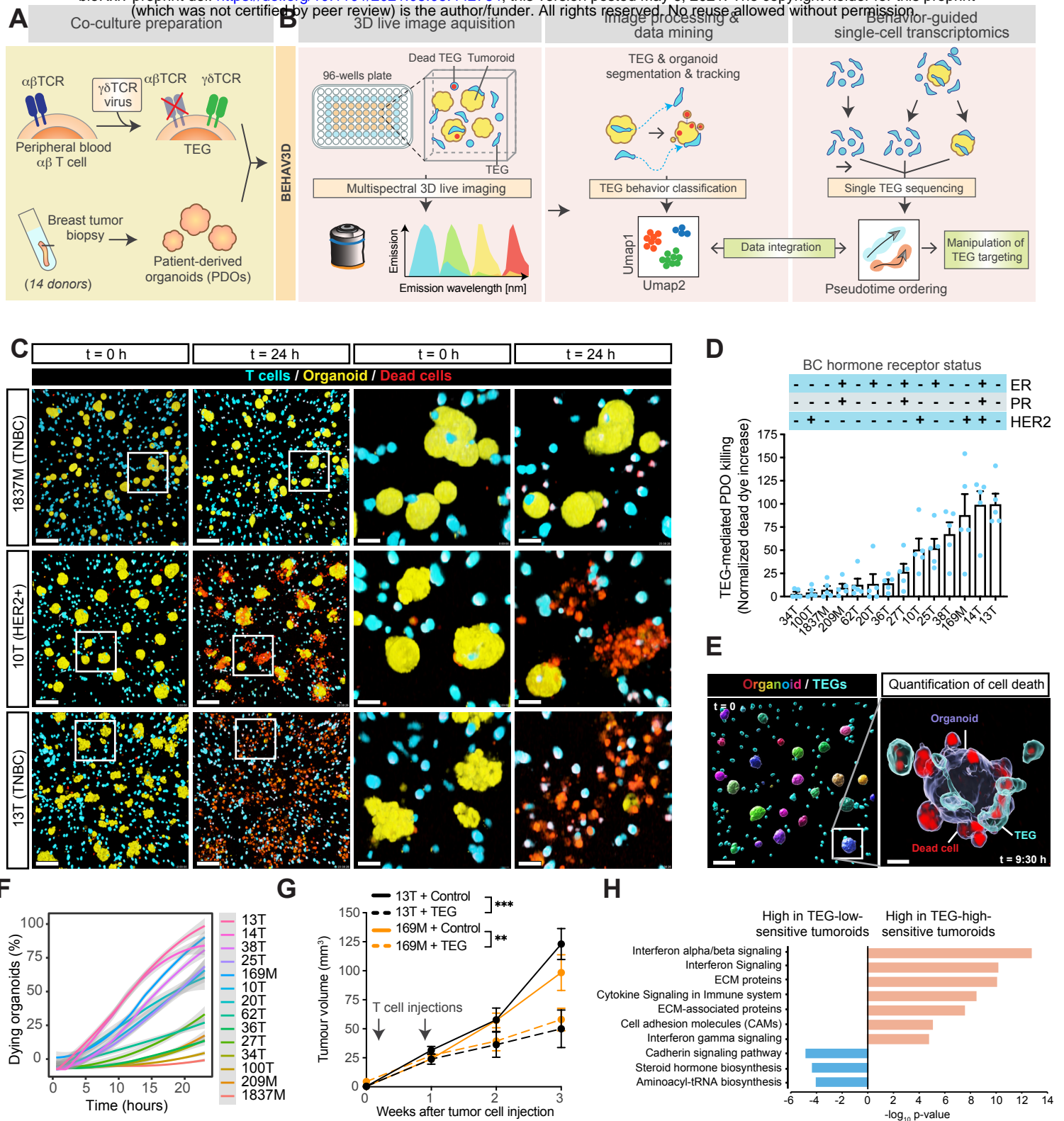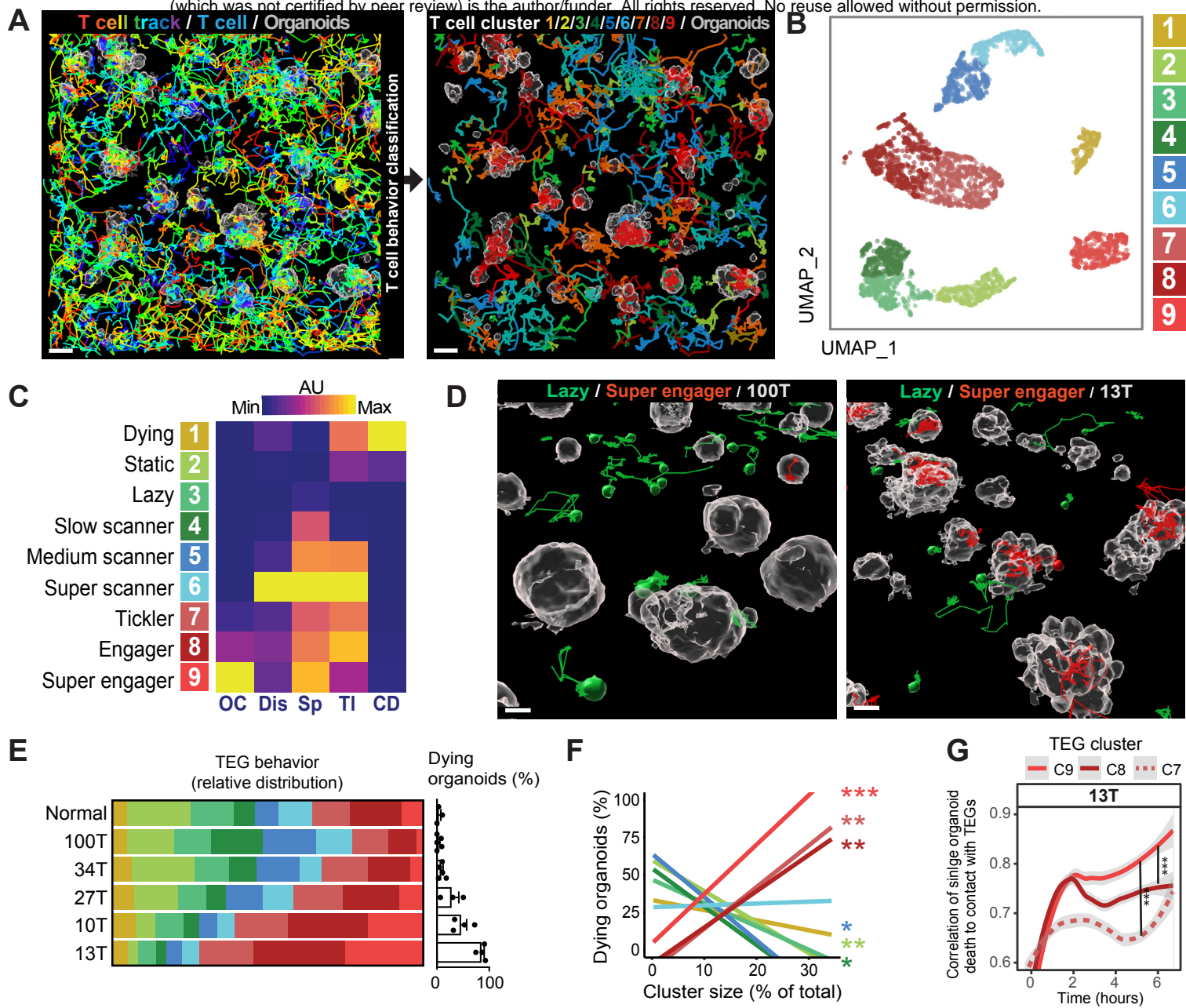
1208   Rectal Cancer. Cell Stem Cell *26*, 17–26.e6.
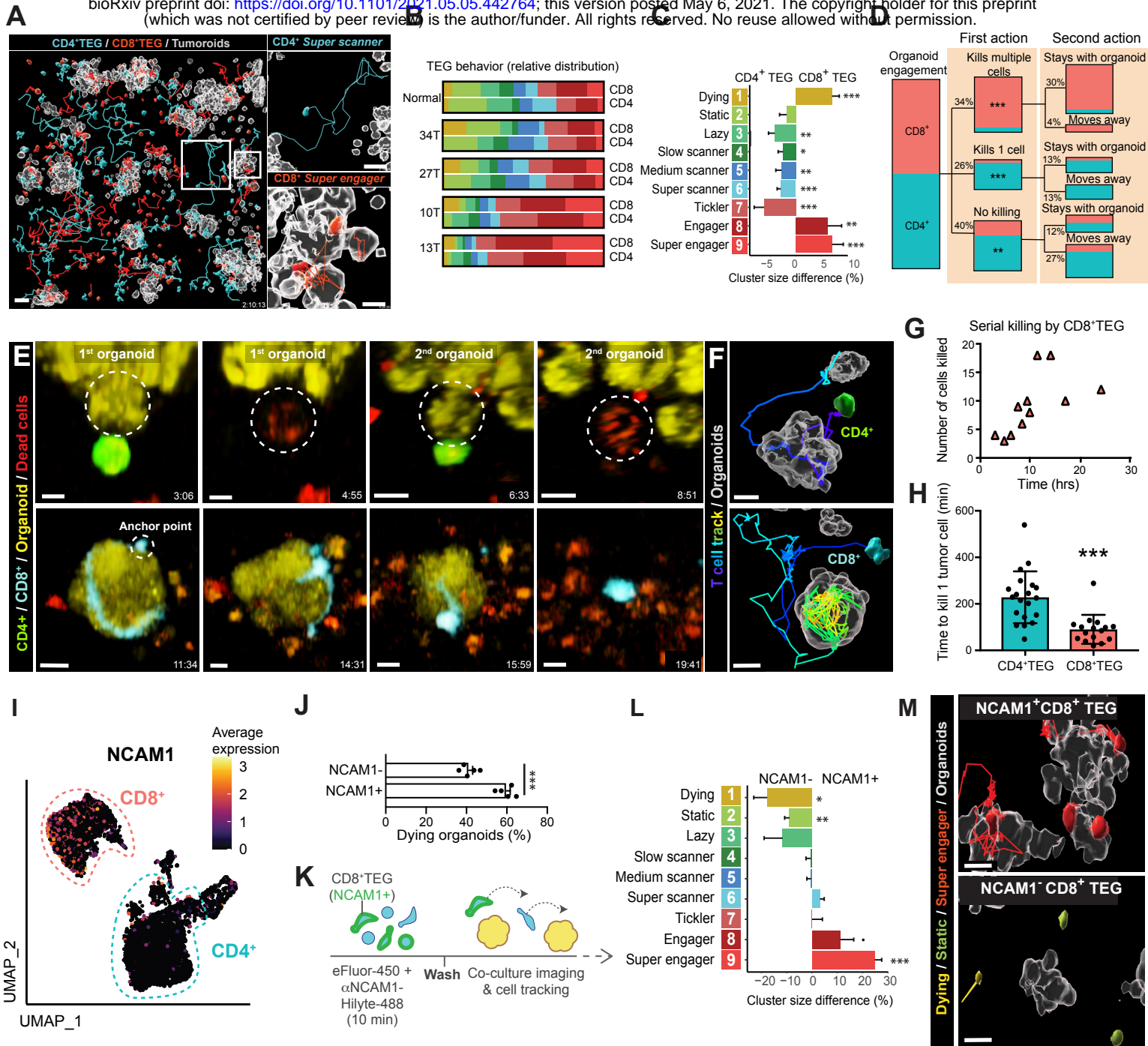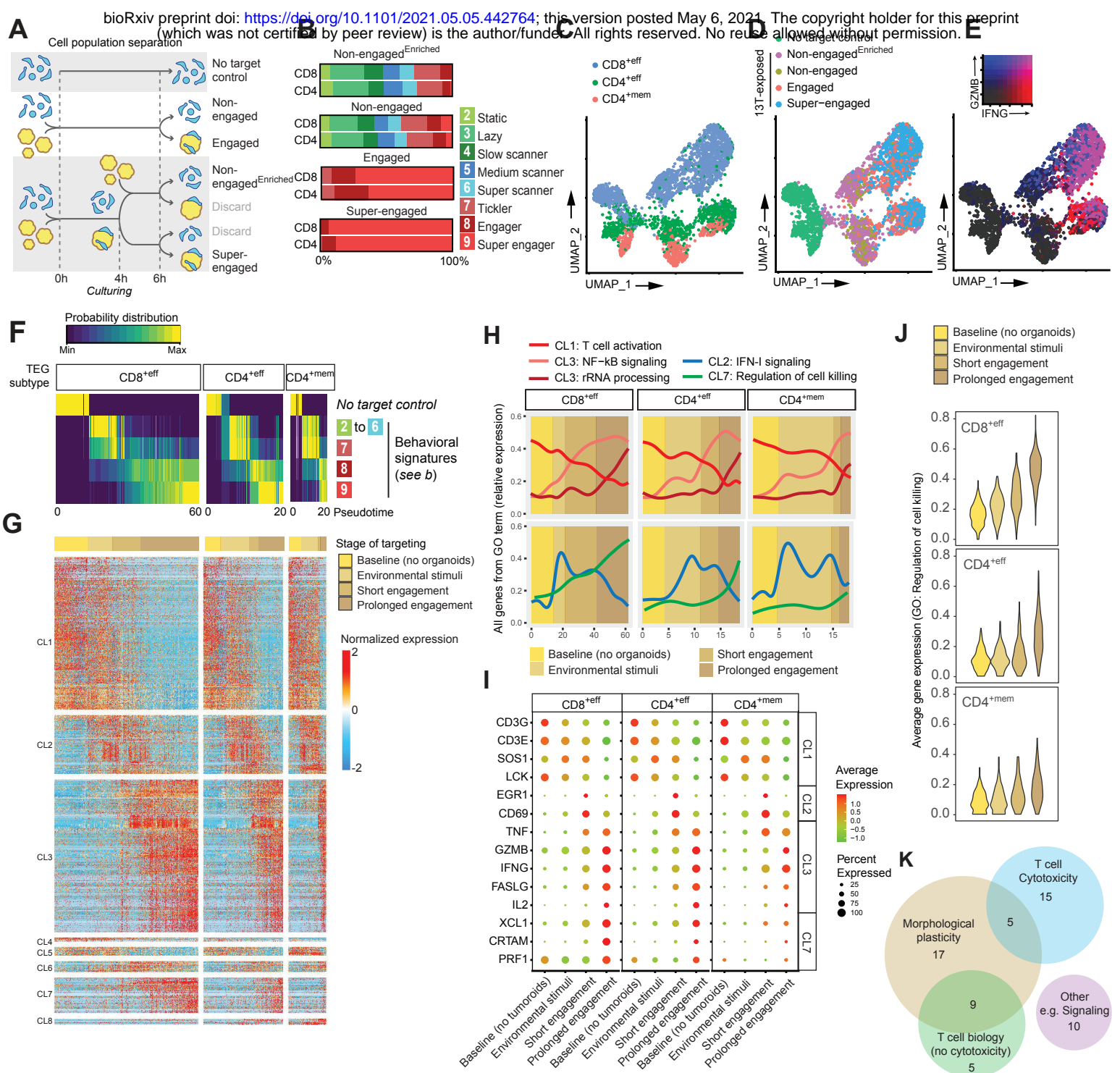
Figure 1

Figure 2

Figure 3

Figure 4

Figure 5